Thiol functionalised gold nanoparticles loaded with methotrexate for cancer treatment: From synthesis to *in vitro* studies on neuroblastoma cell lines

Tommaso A. Salamone [a,*], Lavinia Rutigliano [b], Beatrice Pennacchi [a], Sara Cerra [a], Roberto Matassa [c], Stefania Nottola [c], Fabio Sciubba [d,e], Chiara Battocchio [f], Martina Marsotto [f], Alessandra Del Giudice [a], Andrei Chumakov [g], Anton Davydok [h], Souren Grigorian [a,i], Gianluca Canettieri [b], Enzo Agostinelli [j,k], Ilaria Fratoddi [a,*]

[a] *Department of Chemistry, Sapienza University of Rome, P.le A. Moro 5, 00185 Rome, Italy*
[b] *Department of Molecular Medicine, Laboratory Affiliated to Istituto Pasteur Italia, Fondazione Cenci Bolognetti, Sapienza University of Rome, Viale Regina Elena 291, 00161 Rome, Italy*
[c] *Department of Anatomical, Histological, Forensic and Orthopaedic Sciences, Section of Human Anatomy, Sapienza University of Rome, Via A. Borelli 50, 00161 Rome, Italy*
[d] *Department of Environmental Biology, Sapienza University of Rome, P.le A. Moro 5, 00185 Rome, Italy*
[e] *NMR-based Metabolomics Laboratory (NMLab), Sapienza University of Rome, P.le A. Moro 5, 00185 Rome, Italy*
[f] *Department of Sciences, Roma Tre University, Via della Vasca Navale 79, 00146 Rome, Italy*
[g] *Deutsches Elektronen-Synchrotron DESY, Notkestr. 85, 22607 Hamburg, Germany*
[h] *Institute of Material Physics, Helmholtz Zentrum Hereon, Notkestr. 85, 22607 Hamburg, Germany*
[i] *Institute of Physics, University of Siegen, Walter-Flex-Strasse 3, D-57068 Siegen, Germany*
[j] *Department of Sense Organs, Sapienza University of Rome, Viale del Policlinico 155, 00161 Rome, Italy*
[k] *International Polyamines Foundation "ETS-ONLUS", Via del Forte Tiburtino 98, 00159 Rome, Italy*

GRAPHICAL ABSTRACT

AuNPs-MTX

Methotrexate (MTX)

AuNPs

Neuroblastoma cell

ARTICLE INFO

ABSTRACT

Hypothesis: Colloidal gold nanoparticles (AuNPs) functionalised with hydrophilic thiols can be used as drug delivery probes, thanks to their small size and hydrophilic character. AuNPs possess unique properties for their use in nanomedicine, especially in cancer treatment, as diagnostics and therapeutic tools.

Experiments: Thiol functionalised AuNPs were synthesised and loaded with methotrexate (MTX). Spectroscopic and morphostructural characterisations evidenced the stability of the colloids upon interaction with MTX. Solid state (GISAXS, GIWAXS, FESEM, TEM, FTIR-ATR, XPS) and dispersed phase (UV–Vis, DLS, ζ-potential, NMR, SAXS) experiments allowed to understand structure-properties correlations. The nanoconjugate was tested *in vitro* (MTT assays) against two neuroblastoma cell lines: SNJKP and IMR5 with overexpressed *n*-Myc.

Findings: Molar drug encapsulation efficiency was optimised to be >70%. A non-covalent interaction between the π system and the carboxylate moiety belonging to MTX and the charged aminic group of one of the thiols was found. The MTX loading slightly decreased the structural order of the system and increased the distance between the AuNPs. Free AuNPs showed no cytotoxicity whereas the AuNPs-MTX nanoconjugate had a more potent effect when compared to free MTX. The active role of AuNPs was evidenced by permeation studies: an improvement on penetration of the drug inside cells was evidenced.

1. Introduction

Nanoparticles, especially gold nanoparticles (AuNPs), possess unique properties that make them viable materials for their use in different research fields, *e.g.,* optoelectronics, sensing, catalysis [1–3]. Particularly, gold nanoparticles have a potential for their use in nanomedicine [4] due to their low toxicity, high versatility, and simple synthesis [5–6]. The interest towards their potential use in nanomedicine has grown exponentially, especially in cancer treatment, where AuNPs can be used as different diagnostics and therapeutic tools, often at the same time [7–9]. In the treatment of tumours, small-sized nanoparticles possess unique properties, as they can accumulate in neoplastic tissue through the enhanced permeability and retention (EPR) effect [10]. The different AuNPs functionalisation does indeed open interesting opportunities in the development of bioactive NPs-drugs conjugates, *e.g.,* targeting moieties linked to the surface of the nanoparticles allow to combine the passive targeting, given by EPR, with the active one, given by the functionalisation of the nanoparticles [11–12]. This can be a powerful tool for nanoparticles-based anti-cancer drugs, aimed to obtain multifunctional colloidal nano-systems suitable for both diagnosis and treatment [13–16]. The aforementioned properties of AuNPs can be exploited to obtain nanomaterials suitable in the treatment of cancer, in different applications, such as photodynamic or photothermal therapy, drug delivery and multimodal techniques [17–22]. In the case of drug delivery, the loading of hydrophobic or poorly soluble drugs on AuNPs carriers opens new pathways for the increase of their bioavailability [23].

The comprehension of the interaction in the drug-loaded system is still quite challenging, and the understanding of the loading and release characteristics helps with the system optimisation. The interaction between bioactive compounds and nanoparticles is based on the surface chemistry of the AuNPs. The surface chemistry, in turn, is driven by the presence and nature of the stabilising ligands on the colloidal nano-system [24–25]. Some of the most employed functionalising agents for AuNPs are organic thiols [26], which stabilise the colloidal suspension and functionalise the gold surface by means of an Au–S covalent bond (40 kcal·mol^{-1}) [27]. The choice of covalently bonded capping agents can improve the stability of the colloidal suspension of AuNPs in aqueous and physiological media and allows to obtain versatile materials. Among others, sulfonate and carboxylate groups or aminic moieties determine the surface charge and interfacial chemistry of the nanoparticles, thus allowing to fine tune and select the desired properties for the system [28–30]. Moreover, thanks to the presence and tuning of their optical properties, *i.e.,* the localised surface plasmon resonance (LSPR) phenomenon, it is possible to monitor aggregation equilibria of the colloidal system and improve its stability [31]. In the case of AuNPs for uses in medicine, the surface functionalisation can improve the biocompatibility of the drug, hindering the immune response by the reticuloendothelial system (RES), a problem that "naked", *i.e.,* non-functionalised nanoparticles, do not overcome easily [32]. To enhance the anti-biofouling properties, ligands with high steric and electrostatic properties can be linked to the nanoparticles [33–34]. Different cell lines have been studied in the interaction with drug loaded AuNPs, and among others, neuroblastoma (NB) cell lines represent a starting point for the treatment of neuroendocrine tumours. Neuroblastoma is a tumour that affects mostly children, it accounts for 10% of paediatric

cancers and affects patients in the first 5 years of life; the survival rate does not reach 40% [35].

In this work, we developed a nanoconjugate between methotrexate (MTX), an inhibitor of dihydrofolate reductase (DHFR), and small-sized (diameter lower than 10 nm) hydrophilic gold nanoparticles (AuNPs-MTX). AuNPs are functionalised with two different thiols on the surface, one bearing a negative charge and the other bearing a positive charge, *i.e.,* sodium 3-mercaptopropanesulfonate (3MPS) and 2-(diethylamino) ethanethiol hydrochloride (DEA), respectively. Gold nanoparticles as platforms for MTX delivery have been previously studied [36–37] as well as biopolymer-based colloids [38], although never with a mixed thiol system, where the surface charge plays a fundamental role in the electrostatic interaction between the nanoparticles surface and the drug. Using a nanocarrier to deliver MTX can decrease the negative effects of the drug, which is toxic in higher doses [38]. The appropriate choice of the two ligands can be used to enhance the hydrophilicity and general bioactivity of drug loaded AuNPs [11]. In order to understand and optimise the nature of the interaction, the colloidal AuNPs system before and after the MTX loading has been characterised both in suspension and at the solid state. In particular, UV–Visible, Fourier Transform Infrared Spectroscopy (FT-IR), mono- and bi-dimensional Nuclear Magnetic Resonance (NMR), Dynamic Light Scattering (DLS), ζ-potential, Grazing Incidence Small and Wide Angle X-Ray Scattering (GISAXS, GIWAXS), Small Angle X-Ray Scattering (SAXS), X-Ray Photoelectron Spectroscopy (XPS), Transmission and Field-Emission Scanning Electron Microscopy (TEM, FE-SEM), have been employed to ensure a full characterisation of the loaded and free system.

The loading of MTX on AuNPs was optimised, with a molar drug loading encapsulation efficiency up to 70% depending on different concentrations of AuNPs and drug. Both AuNPs-MTX nanoconjugate and pristine AuNPs, were used to assess the cytotoxic activity for *in vitro* studies and administered to two different neuroblastoma cell lines: SJNKP and IMR5 with overexpressed *n*-Myc.

The small diameter of the AuNPs used in this study can facilitate the permeation inside the blood–brain barrier (BBB), therefore neuroblastoma cell lines were tested [39]. The cell viability was evaluated with the colorimetric assay based on 3-(4,5-dimethylthiazol-2-yl)-2,5-diphenyltetrazolium bromide (MTT), at 24 and 48 h; the functionalised AuNPs did not show any relevant cytotoxicity, whereas the AuNPs-MTX bioconjugate showed an increased cytotoxicity compared to the free MTX drug.

2. Materials and methods

2.1. Materials and reagents

Tetrachloroauric(III) acid trihydrate (HAuCl$_4$·3H$_2$O, 99.0%, M.W. 393.83 g/mol), sodium borohydride (NaBH$_4$, 99.99%, M.W. 37.83 g/mol), methotrexate hydrate (C$_{20}$H$_{22}$N$_8$O$_5$·xH$_2$O, 4-Amino-10-methyl folic acid hydrate, MTX, $\geq$98%, M.W. 454.44 g/mol anhydrous basis), sodium 3-mercapto-1-propanesulfonate (HS(CH$_2$)$_3$SO$_3$Na, 3MPS, 90%, M.W. 178.21 g/mol), 2-(diethylamino)ethanethiol hydrochloride ((C$_2$H$_5$)$_2$NCH$_2$CH$_2$SH·HCl, DEA, 95%, M.W. 169.72 g/mol), 3-(4,5-dimethylthiazol-2-yl)-2,5-diphenyltetrazolium bromide dye (MTT), 4-(2-hydroxyethyl)-1-piperazineethanesulfonic acid 0.1 M (C$_8$H$_{18}$N$_2$O$_4$S, HEPES), ethylenediaminetetraacetic acid tetrasodium salt (C$_{10}$H$_{16}$N$_2$O$_8$, EDTA), Phosphate buffered saline (PBS), dimethyl sulfoxide (DMSO) were used as received from Merck and used without purification. Ultrapure water (H$_2$O$_{up}$, 18.3 MΩ•cm) was produced with a Zeneer Power I Scholar-UV (Full Tech Instruments) deionisation/purification apparatus. Cellulose acetate dialysis tubing with molecular weight cut-offs (MWCO) = 12,000 Da (Merck) were used upon pre-conditioning with distilled water for 12 h.

All cell cultures, flasks, dishes, RPMI-1640 medium and Dulbecco's modified Eagle medium/Ham's F-12 50/50 Mix (DMEM-F12) containing fetal bovine serum (FBS) at 10% (v/v), L-glutamine, 1% Penicillin

(100 IU/mL), Streptomycin (100 µg/mL), without phenol red, were purchased from Corning.

2.2. Cells and cell culture

Two Neuroblastoma (NB) cell lines, *i.e.,* SJNKP (a non-amplified NB cell line) and IMR5 (a n-Myc amplified NB cell line) were used on the basis of previous studies [40]. Both cell lines were a kind gift from Dr. N. Crescenzio (Department of Paediatrics, University of Turin, Regina Margherita Children's Hospital, Turin, Italy) and Dr F. Timeus (Paediatric Haematology-Oncology, Regina Margherita Children's Hospital) [41]. SJNKP and IMR5 cell lines were maintained in monolayer cultures in RPMI-1640 medium supplemented with FBS 10% (v/v), 2 mM L-glutamine, 100 µg/mL streptomycin, and 100 IU/mL penicillin [40]. A humidified atmosphere with 5% CO$_2$ in a water-jacketed incubator at 37C was used for cell incubation. For each passage, exponentially growing SJNKP and IMR5 cells were harvested with EDTA 10 mM and by further addition of trypsin solution 0.10%. Trypsin activity was quenched by the addition of complete RPMI-1640 medium [40]; after centrifuge separation, cells were plated with DMEM-F12. Cells were centrifuged with a Thermo-Scientific centrifuge Megafuge ST Plus Series working at 1,000 rpm (233 g), 2 mins, at room temperature.

2.3. Instruments

UV–Visible. UV–Visible spectra were recorded using a Varian Cary 100 (wavelength range of 190–900 nm) UV–vis spectrophotometer at room temperature. Quartz cells with a 1.5 mL volume and 1 cm optical path length were used. For cell availability test, the multi-mode plate reader spectrophotometer Synergy HT Bioteck was used.

Fourier Transform infrared spectroscopy. FT-IR experiments were conducted with a Bruker Vertex 70. The samples were deposited on KRS-5 cells and analysed from 4000 to 400 cm^{-1}. Spectra in attenuated total reflectance (ATR) mode were recorded in the 4000–600 cm^{-1} range. The resolution is of 4 cm^{-1} with a minimum of 16 scans.

Dynamic light scattering (DLS). The hydrodynamic diameters (<2R$_H$>, nm) and ζ-potentials (ζ-pot, mV) of AuNPs were measured on a Malvern Zetasizer Nano ZS90 instrument at 25 °C using a 4 mW laser light with the wavelength of 632.8 nm and an automatic attenuator. Measurements were done in triplicate and reported as mean $\pm$ standard deviation (SD).

Nuclear magnetic resonance. All NMR spectra were recorded in D$_2$O at 298 K on a Jeol JNM-ECZ 600R spectrometer operating at the proton frequency of 600 MHz and equipped with a multinuclear z-gradient inverse probe head. Monodimensional ^{1}H NMR spectra were acquired with a spectral width of 15 ppm (9013.7 Hz), 64 k data points and 128 scans. The recycle delay was set to 7.7 s to achieve complete resonance relaxation between successive scansions. Bidimensional ^{1}H–^{1}H TOCSY and ^{1}H–^{1}H NOESY spectra were acquired with 96 scans, a spectral width of 15 ppm (9013.7 Hz) in the two dimensions, a data matrix of 8 k $\times$ 256 data points, and a recycle delay of 3 s.

X-Ray photoelectron spectroscopy. XPS experiments were carried out with a homemade instrument, with preparation and analysis ultra-high vacuum (UHV) chambers separated by a gate valve. The analysis chamber contains a six-degree-of freedom manipulator and a 150 mm mean radius hemispherical electron analyser with a five-lens output system and a 16-channel detector giving a total instrument resolution of 1.0 eV as measured at the Ag3d$_{5/2}$ core level. Measurements were carried out on samples deposited onto TiO$_2$/Si(1 1 1) wafers by following a drop-casting procedure; the use of titania substrates allows to avoid signals interference and minimize charging effects due to thick layers of organic molecules. 3MPS and DEA free thiols were drop cast deposited on Au/Si(1 1 1) substrates. Samples were inserted in the preparation chamber and left outgassing overnight at a base pressure of about 10^{-8} Torr, before insertion in the analysis chamber. Vacuum pressure in the analysis chamber during measurements was in the range of 10^{-9}–10^{-10}

Torr. The X-ray radiation is a non-monochromatised Mg Kα (1253.6 eV). C1s signal of aliphatic C atoms having a binding energy of 285.0 eV was used as a reference. Atomic ratio values were calculated from peak intensities. Curve-fitting analysis of the C1s, N1s, O1s, S2p and Au4f spectra was performed using Gaussian profiles as fitting functions, after subtraction of a polynomial background. The $S2p_{3/2,1/2}$ doublets were fitted using the same Full Width at Half-Maximum (FWHM) for both components, a spin-orbit splitting of 1.2 and a branching ratio ($2p_{3/2}$/$2p_{1/2}$) of 1/2. For the $Au4f_{7/2,5/2}$ doublets, a splitting of 3.7 eV, a branch ratio $4f_{7/2}$/$4f_{5/2}$ of 4/3 and the same FWHM values for both spin-orbit components were applied. When several different species were identified in a spectrum, the same FWHM value was set for all individual photoemission bands.

Small-Angle X-ray scattering. SAXS measurements were performed at SAXSLab Sapienza with a Xenocs Xeuss 2.0 Q-Xoom system (Xenocs SA, Sassenage, France), equipped with a micro-focus Genix 3D X-ray Cu source (λ = 0.1542 nm), a two-dimensional Pilatus3 R 300 K detector placed at variable distance from the sample (Dectris Ltd., Baden, Switzerland). The beam size was selected using the two-pinhole collimation system equipped with "scatterless" slits to be 0.5 mm × 0.5 mm. Calibration of the scattering vector q range, where q = (4π sinθ)/λ, 2θ being the scattering angle, was performed using silver behenate. Measurements with two different sample-detector distances were performed so that the overall explored q region was $0.0042 \text{ nm}^{-1} < q < 1.75 \text{ nm}^{-1}$. Samples were loaded into glass capillaries with a nominal thickness of 1.5 mm and sealed with hot glue. They were subsequently placed in the instrument sample chamber at reduced pressure (~0.2 mbar) at 25 °C. The two-dimensional scattering patterns were subtracted for the "dark" counts, and then masked, azimuthally averaged, and normalised for transmitted beam intensity, exposure time and subtended solid angle per pixel, by using the FoxTrot software developed at SOLEIL synchrotron facility. The intensity *vs.* q profiles obtained from the subsequent frames were averaged after checking they were superimposable and were then subtracted for empty capillary and solvent contributions and put in absolute scale units (cm^{-1}) by dividing for the sample thickness estimated by scanning the capillary with the X-ray beam. The different angular ranges were merged using the SAXS utilities tool. The measurements were repeated on the same samples across an overall time of 24 h from the initial loading.

Grazing Incidence Small- and Wide-Angle X-Ray Scattering. GISAXS and GIWAXS measurements were performed at beamline P03 (MINAXS) at the synchrotron PETRA III at Deutsches Elektronen-Synchrotron DESY in Hamburg (Germany) [42]. Samples were prepared by drop casting on SiO/SiO_2 substrate from their aqueous dispersion. X-ray beam with the energy 11.83 keV (wavelength λ = 1.048 Å, Δλ/λ = 10^{-4}) was focused on the detector by beryllium compound refractive lenses (CRL) with a beam size (V × H) $25 × 35 \text{ μm}^2$. Sample-Detector Distance (SDD) was 4190 ± 2 mm for GISAXS and 220.5 mm for GIWAXS. Pilatus 2 M (Dectris Ltd., Switzerland) with the pixel size $172 × 172 \text{ μm}^2$ and pixel array format (V × H) $1475 × 1679 \text{ pix}^2$ was used as a 2D detector for GISAXS mode. GIWAXS 2D images was performed using a Lambda 9 M detector with a pixel size $55 × 55 \text{ μm}^2$. The reciprocal q-space and sample-to-detector distance were calculated using Ag-behenate, CeO and LaB_6 as calibrant. Azimuthally averaged radial distribution of intensity was performed after the analysis of X-ray data using the DPDAK software package [43].

Morphological and Structural studies. Morphology was assessed by an Auriga Zeiss field-emission scanning electron microscope (FESEM) instrument. The samples were drop casted on conducting silicon substrate. Further characterisation was performed by transmission electron microscopy JEOL 2100 LaB TEM operating at 200 kV equipped with an Energy Dispersive X-ray (EDX) detector. AuNPs internalized into IMR5 cells were prepared by a well-established analytical protocol to be observed by Zeiss EM10 TEM [44], operating at 60 kV [45].

2.4. Methods

2.4.1. Synthesis of functionalised gold nanoparticles

The synthesis of gold nanoparticles functionalised with 3MPS and DEA is adapted to the copresence of the 3MPS and DEA thiols, according to a previous study [11], as briefly herein reported for the molar ratio Au/3MPS/DEA = 1/4/10 (hereafter reported as AuNPs). In detail, 0.100 g ($2.54·10^{-4}$ mol) of HAuCl₄ dissolved in 10 mL of H_2O_{up} were added into a 100 mL two-neck round bottom flask. To the gold precursor solution, 0.1811 g ($1.02·10^{-3}$ mol) of 3MPS and 0.4311 g ($2.54·10^{-3}$ mol) of DEA were subsequently added in 10 mL of H_2O_{up} each. The solution was then degassed with Argon under stirring for 10 min; after degassing, 0.0961 g ($2.54·10^{-3}$ mol) of sodium borohydride in 10 mL of H_2O_{up} were added in the flask to reduce the gold and allow for the formation of the functionalised nanoparticles. The reaction was kept under vigorous stirring at room temperature for 2 h. After the 2 h the AuNPs were purified to remove unreacted thiols and by-products from the solution and to isolate smaller nanoparticles: firstly, a centrifuge at 7000 rpm (8910 g) and with a controlled temperature of + 5 °C was performed on the crude mixture to eliminate larger nanoparticles; subsequently, the supernatant (10 mL) was transferred to a dialysis tube for purification with distilled water (500 mL) for 7 days under mild agitation at room temperature, removing the external water and adding fresh distilled water at a regular interval of time of 24 h.

Physical and spectral data of pristine AuNPs (molar ratio 1:4:10). UV–Vis (H_2O): $λ_{max}$ = 520 nm; <2R_H> (DLS, H_2O): (9 ± 2) nm; yield: 29 ± 8 %wt; FTIR (ATR, solid): ν = 3060 (w), 3020 (w), 1584 (m), 1472 (s), 807 cm^{-1} (s).

2.4.2. Loading and release of methotrexate on AuNPs

Methotrexate was loaded on AuNPs for the use of the nanoconjugate in *in vitro* tests to assess their cytotoxicity. Based on previous reports [36], the concentrations of AuNPs used were 0.5, 10, 50 μg/mL with AuNPs/MTX weight ratio of 1/20, 1/1 and 5/1, respectively. The loading of MTX on AuNPs 50 μg/mL is briefly reported as an example. A stock solution (400 μg/mL) of MTX in 0.1 M HEPES buffer, was diluted in deionised water to 120 μg/mL and 500 μL of this solution are added – under stirring – to a round bottom flask containing 500 μL of an aqueous solution of AuNPs at a concentration of 600 μg/mL; the mixture was allowed to react, under stirring, in the dark at room temperature for 2 h. After 2 h, the solution is inserted in a dialysis membrane and put in 100 mL of distilled water for 30 min under stirring at room temperature to allow for the free MTX to be released from the membrane into the outside water. The AuNPs-MTX nanoconjugate (AuNPs concentration is 300 μg/mL) is then stored at −18 °C to avoid the release of the drug. To obtain AuNPs 50 μg/mL for *in vitro* tests, the AuNPs-MTX conjugate was diluted in 3 mL of DMEM-F12. To evaluate the free MTX and thus the loading of the drug on the nanoparticles, the outside solution is collected, and the water is removed via rotary evaporation. The recovered MTX is dissolved in 3 mL of HEPES buffer 0.1 M, and its quantity is evaluated via UV–Vis, comparing the absorbance at λ = 303 nm result with a calibration curve, reported in the Supporting Information, Figure S1).

Molar Drug Loading Encapsulation Efficiency (η%) and Drug Loading (L%) were calculated following eqs (1) and (2), respectively [46]:

Molar Drug Loading Encapsulation Efficiency (%) = η%

$$= \frac{mol_{MTX_{AuNPs}}}{mol_{MTX_{initial}}} \cdot 100 \qquad (1)$$

where $mol_{MTX_{AuNPs}}$ is the molar quantity of MTX loaded onto AuNPs, $mol_{MTX_{initial}}$ is the molar quantity of MTX initially added in the formulation.

$$Drug\ Loading\ (\%) = L\% = \frac{w_{MTX_{AuNPs}}}{w_{AuNPs\_MTX}} \cdot 100 \qquad (2)$$

where $w_{MTX_{AuNPs}}$ is the mass quantity of MTX loaded onto AuNPs, and w_{AuNPs_MTX} corresponds to the mass quantity of AuNPs-MTX nanoconjugate.

Release was studied following the ζ-potential signal. An AuNPs-MTX solution was left to stir mildly for 48 h at room temperature; after 2 and 4 h a 1 mL sample was collected and measured, after 48 h the stirring was stopped, and 1 mL of the solution was measured.

2.4.3. Cell viability and permeation studies

Pristine and MTX-loaded AuNPs were tested on NB cell lines and results compared with free MTX drug. SJNKP and IMR5 cells at a concentration of 5,000 cells per well, were seeded in 96-multiwell plates and treated for 24 and 48 h with three different concentrations of gold nanoparticles, named as AuNPs (pristine) 0.5 μg/mL, AuNPs 10 μg/mL and AuNPs 50 μg/mL and AuNPs-MTX with a (17 ± 5) μM of MTX. Low concentrations of MTX on AuNPs were also used to treat cells for 48 h (0.015, 0.031, 0.124 μM on AuNPs 0.5 μg/mL, 10 μg/mL, 50 μg/mL, respectively). Cells were treated with unloaded nanoparticles and free drug separately, as a control. After 24 and 48 h, growing medium was discarded and replaced with MTT solution to assess the cell viability [47]. MTT reading wavelength was set at 577 and 660 nm, then

processed according to Kanamori et al. [40,48]. Cell viability was analysed by GraphPad Prism and reported as % of viable cells, where control cells are 100 %.

To assess the permeation of nanoparticles inside the cells, for the highest concentration (50 μg/mL) the growing medium was separated and analysed *via* UV–vis. The absorbance of AuNPs and AuNPs-MTX inside the separated growing medium was compared to the 50 μg/mL stock solution of AuNPs. Permeation % (P%) was calculated as follows in eq (3):

$$\text{Permeation} \,(\%)\,P\% = 100 - \frac{Abs_0}{Abs_i} \bullet 100 \tag{3}$$

where Abs_0 is the absorbance value at 515 nm of the AuNPs stock, and Abs_i is the value of the AuNPs or AuNPs-MTX solutions after the treatment at 24 or 48 h.

MTT assays were carried out least three times for statistical analysis and results were expressed as mean values $\pm$ SD. The Student's *t*-test was used to analyse the statistical significance and differences between the test and control groups were considered to be significant at *p < 0.05 and very significant at **p < 0.01. One-way Anova, Dunnett's and Sidak's multiple comparisons test were performed for statistical
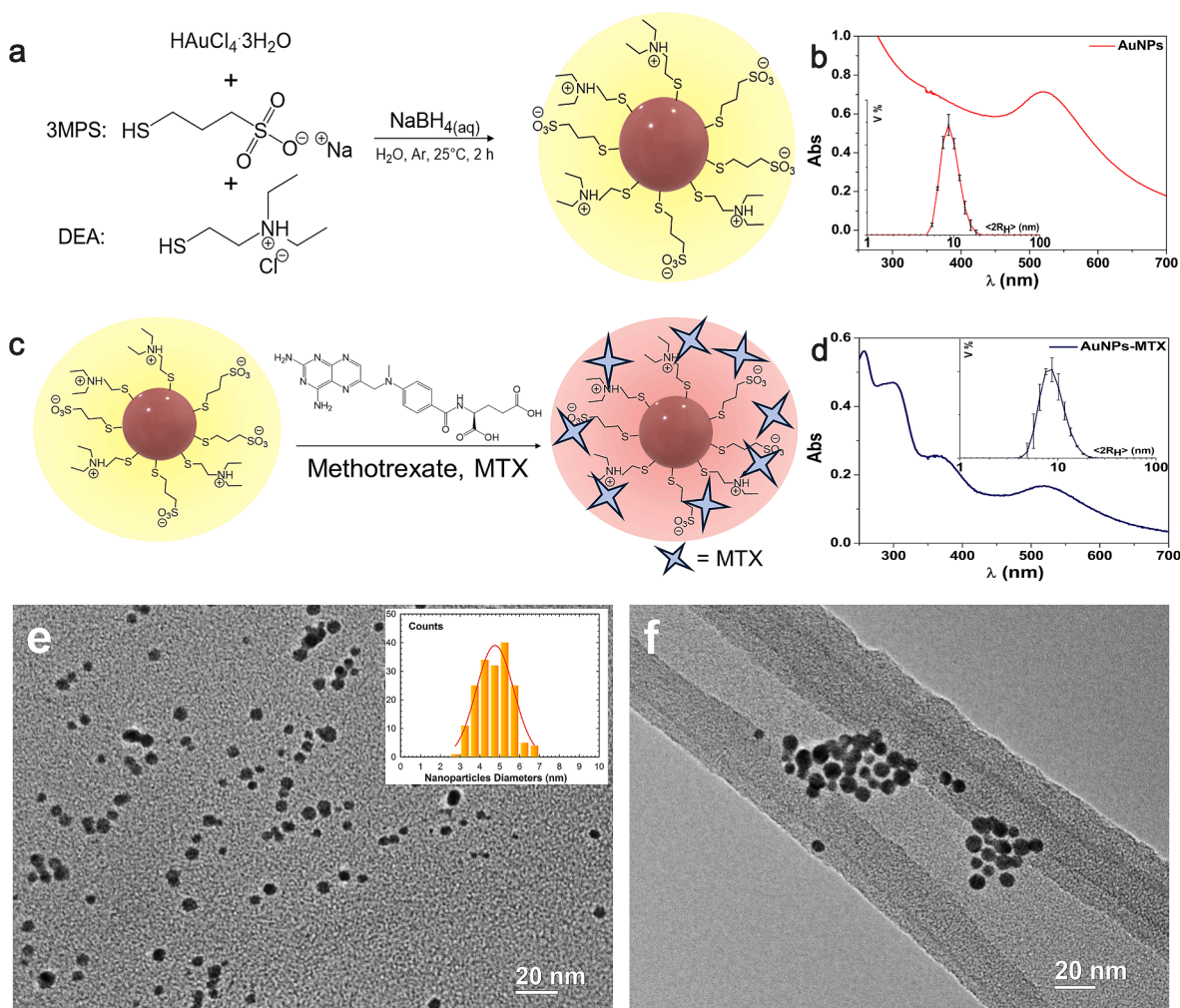

Fig. 1. a: Schematic depiction of the AuNPs synthesis process; b: UV–Vis spectrum of pristine AuNPs in H_2O_{up} at concentration 50 μg/mL ($\lambda_{max} = 520$ nm). Inset: Hydrodynamic size distribution of pristine AuNPs at concentration 50 μg/mL ($<2R_H> = (9 \pm 2)$ nm); c: Schematic representation of MTX loading on AuNPs to obtain AuNPs-MTX; d: Spectroscopic characterisation of AuNPs-MTX nanoconjugate in H_2O_{up} at concentration AuNPs 10 μg/mL loaded with 17 μM of MTX ($\lambda_{max} = 520$ nm). The band associated with MTX has a maximum at 303 nm, in accordance with literature reports [52]. Inset: Hydrodynamic size distribution of loaded AuNPs-MTX nanoconjugate (AuNPs 10 μg/mL and MTX 17 μM), ($<2R_H> = (9 \pm 3)$ nm). e,f: morphological observations of AuNPs and their non-covalent self-assembling of AuNPs-MTX. e: High resolution TEM image of AuNPs. Inset: frequency distribution of the nanoparticles size and data fitted by Gaussian function (red line). f: HR-TEM images of single nanoconjugates. (For interpretation of the references to colour in this figure legend, the reader is referred to the web version of this article.)

analysis.

3. Results and discussion

Synthesis of gold nanoparticles functionalised with 3MPS and DEA mixed thiols and AuNPs-MTX was carried out following a wet reduction procedure in water [49], using two hydrophilic thiols in mixture, as previously described in section 2.4.1 and schematically shown in Fig. 1a. In detail, it is a bottom-up wet reduction method, where 3MPS and DEA thiols are used in mixture as capping and functionalising agents, and sodium borohydride is added as the reducing agent. The synthesis employed in this work is done in mild conditions, at room temperature and atmospheric pressure; it is noteworthy that the reagents are non-toxic, and the reaction is carried out with water as a solvent. Different molar ratio between Au precursor and the two thiols were tested and, in this work, we focussed on the Au/3MPS/DEA = 1/4/10 M ratio. The synthesised gold nanoparticles were extensively characterised both before and after the interaction with MTX. Subsequently, *in vitro* cell viability tests were carried out to deeply define the structure of the nanocarrier and its modifications upon the drug loading, as schematically reported in Fig. 1c, as well as studying the interfacial interaction between the surface of the nanoparticles and MTX.

3.1. Basic and advanced characterisation of pristine AuNPs and AuNPs-MTX nanoconjugate

After careful purification of the AuNPs, small sized AuNPs were obtained, as evidenced by UV–visible and DLS measurements of AuNPs, shown in Fig. 1b and its inset. The wavelength value of the maximum of the local surface plasmon resonance (LSPR) band provides an indication of the size of the gold nanoparticles, whereas the broadness of the band indicates the dispersity of the sample. In Fig. 1b, the LSPR band is centred at 520 nm, which suggests that the mean diameter of the gold nanoparticles should be of ca. 10 nm [50]. This value is in fact in accordance with the DLS measurements shown in the inset of Fig. 1b which reflect a hydrodynamic diameter equal to $<2R_H> = (9 \pm 2)$ nm. The small size, high surface area and low polydispersity, together with the hydrophilic external layer, play a key role in the possibility to use these materials for drug delivery. Therefore, these features improve the loading efficiency of the hydrophobic drug, while also avoiding non-specific accumulation in organs and favouring clearance through the kidneys [51]. To assess their long-term stability at 37 °C in DMEM-F12 culture medium, UV–Vis studies in time were carried out. The aggregation dynamics can be studied by following the shift of the λ_{LSPR} over time; it was found that the aggregation over 14 days was noticeable in the first two days, with a wavelength value of 520 nm for the pristine AuNPs, which increased to only 528 nm after 2 days in DMEM-F12 at 37 °C and stayed stable at that value up to 14 days (Figure S2).

MTX was loaded on AuNPs following the method described in section 2.4.2, thus obtaining the AuNPs-MTX nanoconjugate. Concerning the UV–vis spectrum (Fig. 1d), it indicates no significant aggregation due to the presence of MTX, as the λ_{LSPR} is centred at around 520 nm, the same values as before the interaction with the drug (*cfr.* Fig. 1b). The three MTX bands appear at lower wavelength values (260, 303, and 370 nm), and the one at λ_{max} of 303 nm was used as a marker. In the inset of Fig. 1d, the DLS graph is reported, and, similarly to the UV–visible measurements, it indicates that no relevant aggregation occurred after the MTX loading. The mean hydrodynamic diameter of AuNPs-MTX is $< 2R_H> = (9 \pm 3)$ nm, whereas the DLS of pristine AuNPs showed a hydrodynamic diameter equal to $< 2R_H> = (9 \pm 2)$ nm (*cfr.* Inset of Fig. 1b).

To have a better understanding of the size and shape of the nanoparticles, Fig. 1 e,f show electron microscopy images of the system before and after the interaction with MTX. Single AuNPs were observed by high resolution TEM and they have shown a diameter of (4.76 ± 0.09) nm in average (Fig. 1e and inset). After non-covalent interaction

with MTX, the AuNPs maintain their structure and size with limited interactions between particles, as HR-TEM images of AuNPs-MTX nanoconjugates show (Fig. 1f). The size difference (ca. 5 nm) between a solvent mediated measurement such as DLS and a solid-state technique such as HR-TEM is due to the fact that DLS takes into account the presence of the thiols surrounding the metal core, as well as the solvation shell, whereas with electron microscopy studies, only the metal core can be measured. FESEM images of AuNPs and AuNPs-MTX are shown in Figure S3.

To evaluate the possibility of the use of the system as a drug nanocarrier, the *Molar Drug Encapsulation Efficiency (η%)* and *Drug Loading (L %)* were studied, evaluating the quantity of loaded MTX via UV–Vis with the calibration curve of MTX ($R^2 = 0.9994$; $\varepsilon_0 = (20,540 \pm 2630)$ M^{-1} cm^{-1}) (Figure S1) [53]. The obtained *η%* was optimized to be 70% by using the AuNPs/MTX 5:1 wt ratio, testing the loading in different AuNPs/MTX weight ratios as reported in Figure S3 and Table S1, together with qualitative UV–vis overlapped spectra of MTX, AuNPs and AuNPs-MTX samples. The samples used for the cell studies were the 1/20, 1/1 and 5/1 wt/wt ratios, with respective final concentrations of nanoparticles of 0.5 μg/mL, 10 μg/mL, and 50 μg/mL.

The nanoconjugate AuNPs-MTX, as well as the pristine AuNPs have been characterised more in depth in order to assess the nature of the interaction and its influence on the structure of the nanomaterial. Fourier transform infrared spectroscopy proved to be useful to assess the structure and to investigate the nature of the interaction between the drug and the gold nanoparticles. The spectra were collected in the attenuated total reflectance mode (ATR) on the dry samples. The FTIR spectrum of pristine AuNPs-3MPS-DEA (Fig. 2a) exhibits the typical asymmetric stretching (ν_{as}) of $-SO_3^-$ at 1027 cm^{-1} and symmetric stretching (ν_s) of $-SO_3^-$ at 1150 cm^{-1} related to the presence of 3MPS on AuNPs surface. Being a tertiary amide the are no absorption associated with $-N(CH_3)_2$ of DEA, whereas C—N stretching vibration is partially overlapped with $\nu_{as}(-SO_3^-)$ at 1027 cm^{-1}. Asymmetric stretching of $-CH_2$ and $-CH_3$ can be found at 2920 and 2978 cm^{-1}, respectively. Thiol related carbon sulphur single bond stretching resonates at 718 cm^{-1}. Fig. 2b shows the superimposed spectra of drug loaded AuNPs and free MTX (blue and dark red lines, respectively) and the FTIR spectra of free 3MPS and DEA thiols are reported in Figure S4. A shift in characteristic MTX bands before and after the interaction with the surface thiols on the AuNPs is observed in the ATR spectra. The shifts can help to interpret the nature of the chemical interaction between MTX and thiols functional groups. The infrared spectrum of pristine MTX (dark red) highlights the presence of the typical C=O stretching band of the carboxylic acid at 1643 cm^{-1}, at 1596 cm^{-1}, the aromatic skeletal stretching vibrations give rise to a strong band, whereas the aromatic out of plane bending band is centred at 830 cm^{-1} [54]. In the AuNPs-MTX spectrum (blue line), the corresponding bands are shifted towards lower wavenumber values, the carboxylic acid band shifts to 1589 cm^{-1}, whereas the aromatic stretching band shifts to 1557 cm^{-1}; the out of plane bending band does not shift notably. The vibration bands pertaining to the C=O stretching and to the aromatic stretching are shifted considerably, for the C=O band, $\Delta\nu$ = -54 cm^{-1}, for the aromatic band, $\Delta\nu$ = -39 cm^{-1}. An interaction between carboxyl group and aromatic group pertaining to MTX and the end group functionalities of the thiol ligands can be envisaged.

In order to have structural information, XPS measurements were carried out at the C1s, N1s, O1s, S2p and Au4f core levels on pristine AuNPs, free MTX, AuNPs-MTX, DEA and 3MPS deposited following a drop-casting procedure onto proper substrates. C1s, O1s, N1s, Au4f and S2p spectra were analysed following a peak-fitting procedure, allowing to individuate the components arising by chemical elements with different atomic environment (*i.e.*, in different functional groups); all peak positions BE (Binding Energies), Full-Width at Half Maximum (FWHM) values, atomic ratios (relative intensities) and assignments are reported in Supporting Information Tables S2-S6 and C1s spectra of AuNPs, MTX, AuNPs-MTX, DEA and 3MPS are reported in Figures S10-
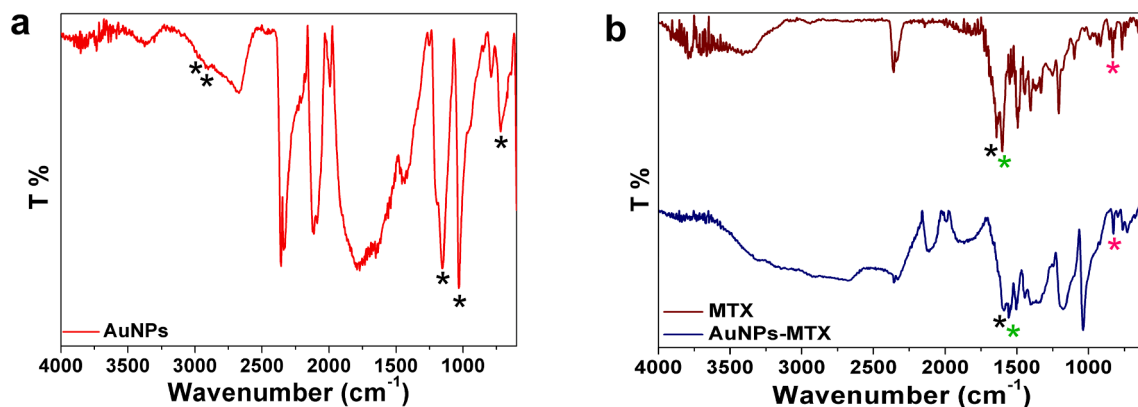
Fig. 2. a: FTIR spectrum of pristine AuNPs-3MPS-DEA. Relevant bands are marked with and asterisk. b: FTIR superimposed spectra of AuNPs-MTX nanoconjugate (blue) and MTX (dark red). C=O stretching band is marked with a black asterisk, the green asterisk represents the skeletal aromatic stretching band, and the magenta asterisk is used for the out of plane aromatic bending. Spectra were recorded in ATR mode on solid samples. (For interpretation of the references to colour in this figure legend, the reader is referred to the web version of this article.)

S13. The most interesting signals to evaluate the AuNPs stability and interaction with MTX are Au4f, S2p and N1s core levels, and they will be here discussed in detail.

Au4f core level spectrum of AuNPs (Figure S10, Table S2) is composed of two spin–orbit doublets (Au4f$_{7/2}$, Au4f$_{5/2}$); the more intense Au4f$_{7/2}$ component, due to metallic Au (0) atoms, is usually taken as reference (BE = 83.9 eV). As expected for small nanoparticles, the high surface to volume ratio allows us to observe also the Au4f signal related to substrate-thiol interface atoms: the spin–orbit pairs at higher BE values (Au4f$_{7/2}$ = 84.9 eV) appear as a pronounced shoulder on all the Au4f measured spectra [55]. N1s spectrum of pristine AuNPs (Fig. 3a) has two components both indicative of DEA presence and stability: a main signal at 399.9 eV due to amine terminal groups of DEA thiol, and a small peak at 401.6 eV usually attributed to charged amine groups [56].

N1s spectrum of MTX (Fig. 3b) shows a single peak related to aliphatic and aromatic amine groups, centred at 400.9 eV. Au4f core level spectrum of AuNPs-MTX (Figure S11, Table S3), in analogy with the pristine sample shows the two spin–orbit doublets (Au4f$_{7/2}$, Au4f$_{5/2}$) with the Au4f$_{7/2}$ component centred at 83.7 eV for Au(0) and 84.7 eV attributed to Au($\delta+$) atoms on the surface covalently linked to sulphur atoms.

Looking at S2p spectra reported in Fig. 3d, the B.E. value of S2p$_{3/2}$ signal, taken as a reference for the S2p$_{3/2-1/2}$ spin–orbit pair, proves whether the sulphur atom is linked to the metal surface with a covalent bond or not. For thiols covalently anchored on metals, as well as on metal nanoparticles surface, an S2p$_{3/2}$ BE value of *circa* 161.5 eV is expected; S2p$_{3/2}$ signals around 163 eV are usually assigned to non-
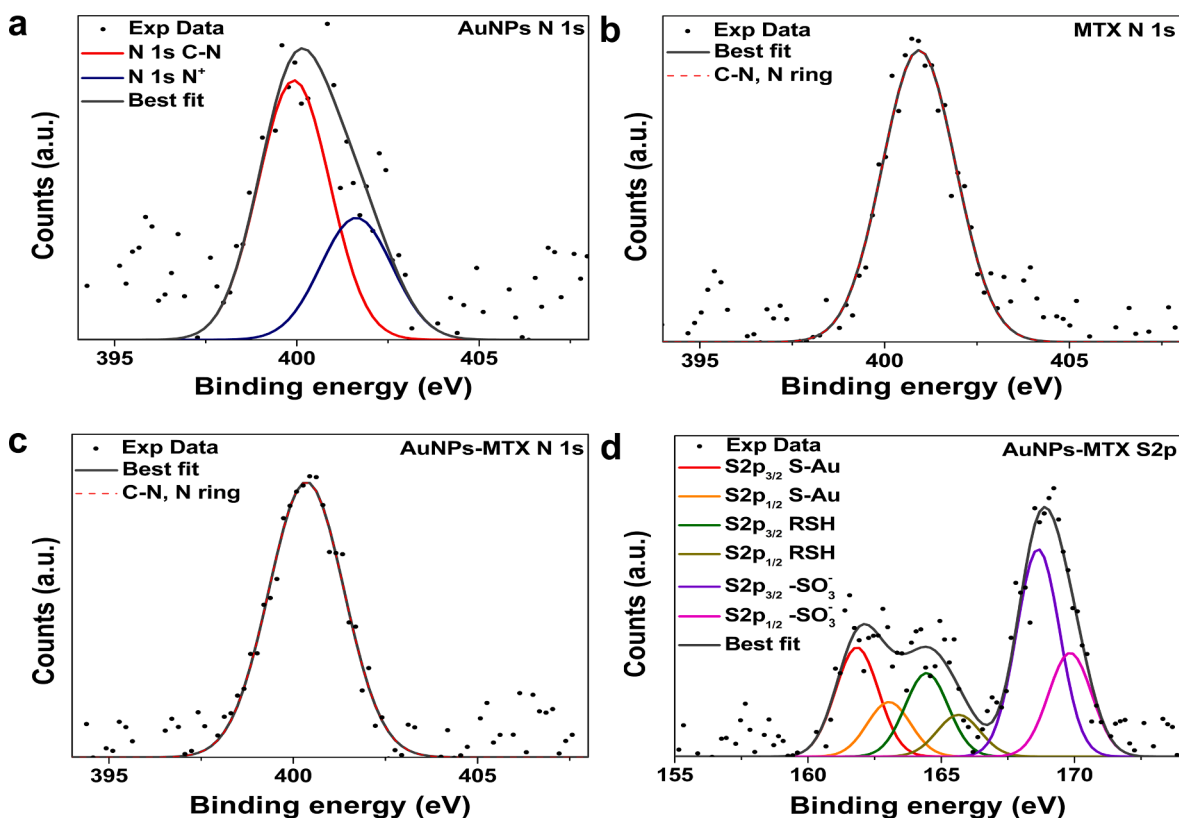

Fig. 3. XPS spectra of a, AuNPs at N1s core level; b, MTX at N1s core level; c, AuNPs-MTX at N1s core level; d, AuNPs-MTX at S2p core level.

covalently bonded thiols or thiolates [56]. Both components are observed for conjugated nanoparticles sample, suggesting that the thiol interaction with gold atoms at NPs surface is stable and not affected by the AuNPs functionalization with MTX. The S2p signal component at high BE (S2p$_{3/2}$ BE around 168 eV) arises from the sulphonate end-group of 3MPS.

AuNPs-MTX N1s spectrum (Fig. 3c) only has one component at 400.3 eV associated to C—N and *N*-ring nitrogen, as does the MTX N1s spectrum (Fig. 3b), centred at 400.9 eV. The absence of the signal pertaining to the charged amine of DEA, and the presence of only the MTX-related signal can be interpreted as further evidence of an electrostatic interaction between MTX and the charged group functionalities of AuNPs, specifically the charged terminal amine of DEA. Furthermore, the slight shift in BE (0.6 eV) shown in the N1s spectrum related to the MTX before and after the interaction with the gold nanoparticles could support the hypothesis of a cation-π interaction between the charged moiety of DEA and the aromatic rings of MTX.

The permanence of all MTX-related signals in AuNPs-MTX systems indicates that MTX molecules interact with AuNPs with weak chemical forces, then the molecular structure and functional groups of MTX are fully conserved in the adduct formation. The presence of weak interactions between the drug and the thiols on the AuNPs surface suggests that methotrexate could maintain its biological activity.

The ζ-potential of AuNPs provides information on the surface charge of the nanoparticles. In Fig. 4, a study over time of the ζ-potential of AuNPs is reported. The gold nanoparticles used in this study are functionalised with the two thiols, which at pH = 7 exhibit two charges, a negative (3MPS) and a positive (DEA) one [57–58]. As a consequence of the two charges on the AuNPs, the surface charge is a result of the net sum of the two. The value of the ζ-potential was found equal to (-16 ± 1) mV, in accordance with the presence of the different charges, as opposed to AuNPs functionalised with only 3MPS, which typically exhibit a ζ-potential of ca. −30 mV [36], and with only DEA where the ζ-potential value is at ca. + 30 mV [56]. As shown in Fig. 4, after 40 min, the value reaches a minimum of ζ-potential = (-40 ± 1) mV, and subsequently, after 60 min and for the remaining hour of the reaction sets to a value of around −30 mV, with a final value at 2 h of ζ-potential = (-27 ± 2) mV. After the loading, the release of the drug from the AuNPs was evaluated, with the value of the ζ-potential increasing to (-21 ± 2) mV after 4 h and

reaching the value (-11 ± 5) mV after 48 h, which could be ascribed to a complete release of MTX loaded on AuNPs. The ζ-potential trend during the loading and release processes indicates that the positive charge on the surface of the AuNPs is partially shielded by the presence of MTX. This suggests that the interaction between the nanostructure and the drug is mainly driven by DEA-methotrexate interaction.

To further investigate the surface chemistry and stoichiometric ratio between the thiol ligands, NMR studies were carried out on AuNPs. Fig. 5a shows a detail of the ¹H spectrum of AuNPs (for full spectra *cfr.* Figure S5), where the presence of both thiols on the surface of the nanoparticles can be confirmed, as the signals of the central methylene of the aliphatic chain of 3MPS and the signal of the terminal methyl groups of DEA thiol can be distinguished (δ = 2.18 ppm and δ = 1.43 ppm, respectively). The signals at higher fields that are visible on the spectrum pertain to the free thiol in solution, unbound on the nanoparticle surface [59]. This observation is in agreement with literature reports, where physically sorbed thiols are often found even after purification [60]. By comparing the integrals of these two signals, the molar ratio between the two thiols on the surface of the nanoparticles can be calculated; it was found to be ca. 1/2 in favour of 3MPS, in accordance with the negative ζ-potential value of the system (*cfr.* Fig. 4).

In order to understand the interaction with the drug in the loaded samples, NMR studies were carried out on AuNPs-MTX and compared with free MTX. Fig. 5c is a superimposition of the ¹H spectra of methotrexate (dark yellow) and AuNPs-MTX (blue); the inset is a detail of the aromatic portion of the spectrum, where only signals pertaining to the drug are present. In the rest of the spectrum, no visible difference in the chemical shift of the MTX related signals can be seen, whereas, in the 6.90–8.70 region a clear shift in the two doublets and one singlet aromatic signals of MTX is evident. The chemical shift values before and after are: δ = 8.64 ppm, before the interaction, δ = 8.60 ppm, after the interaction; δ = 7.76 ppm before, δ = 7.72 ppm after; δ = 6.94 ppm before and δ = 6.90 ppm after. All the MTX aromatic proton signals are more shielded than before when the drug is loaded on the surface of the nanoparticle; as this is the only significant shift in the ¹H NMR spectra, it can be inferred that the aromatic portion of methotrexate is directly involved in the interaction with the thiols on the surface of the nanoparticles, presumably with the positively charged portion of DEA [61].

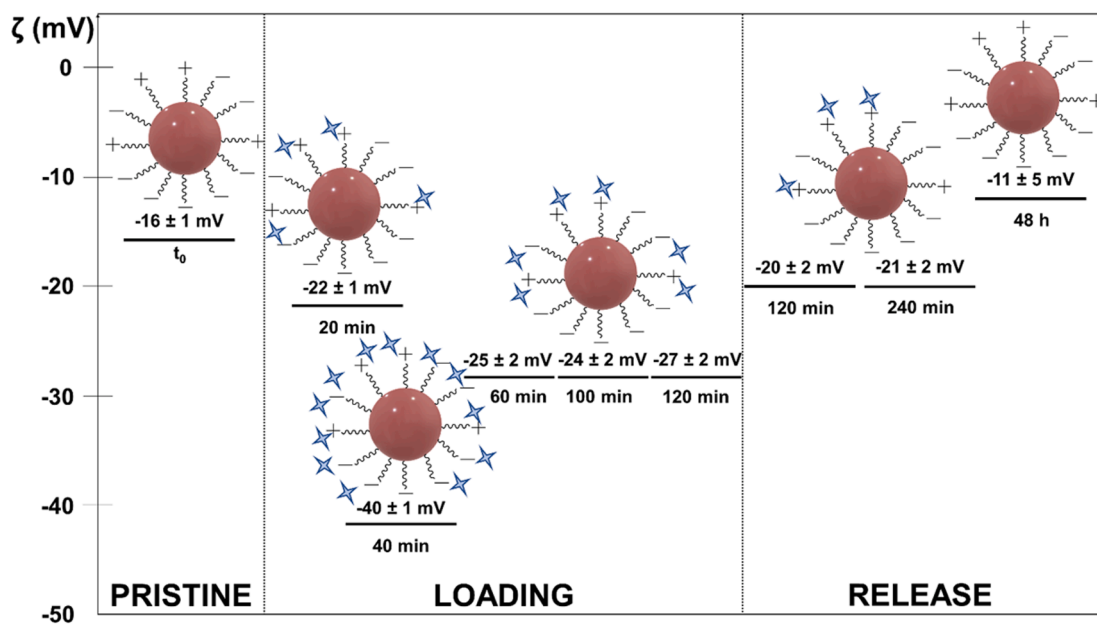These analyses support the hypothesis that the interaction between

Fig. 4. Study of the surface ζ-potential in H$_2$O$_{up}$ of pristine, loaded and released AuNPs (AuNPs/MTX 5/1 wt/wt), at different time points during the loading (every 20 min up to 2 h) and release (after 2, 4 and 48 h) process. The blue star represents MTX. The ζ-potential measurements of AuNPs at different time points are reported in Figure S3.
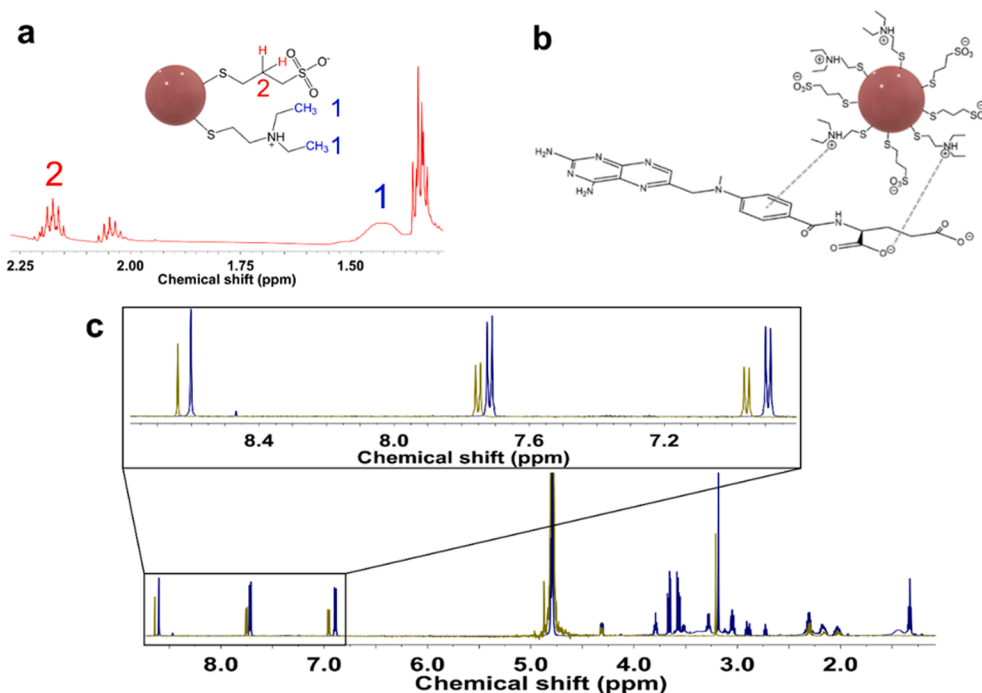
Fig. 5. ^{1}H NMR spectra of a, pristine AuNPs; inset: AuNPs and surface thiol structure; b: chemical structure illustrating the AuNPs-MTX interaction; c: ^{1}H NMR superimposed spectra of AuNPs-MTX (blue) and MTX (dark yellow) alone (also reported in Figure S5); inset: aromatic portion of the spectra. The solvent of all spectra is deuterium oxide (4.76 ppm, broad).

the drug and the AuNPs is of twofold nature: electrostatic, through the interaction of the carboxylate groups of MTX and the ammonium of DEA, and also a cation-π interaction between the ammonium and the aromatic moiety of MTX [62], as schematised in Fig. 5b). By comparison with our previous results on AuNPs functionalised with 3MPS alone, the system used in this work shows an enhanced interaction with the positively charged of the DEA thiol on the AuNPs. Moreover, the formation of small sized and stable colloidal suspensions also upon MTX interaction makes the AuNPs stabilised with DEA and 3MPS in mixture particularly suitable for nanomedicine.

3.2. X-ray scattering analysis

Small angle X-ray scattering (SAXS) measurements allowed to characterise the size and shape in solution of the as-synthesised nanoparticles and of the AuNPs-MTX nanoconjugate. Fig. 6 shows the scattering profiles of AuNPs and of AuNPs-MTX (Fig. 6a) and the best fits according to a homogeneous sphere model with a lognormal distribution of the radius (in the lower inset), in accordance with the expected spherical shape of the AuNPs. The obtained values of the average radius and distribution width were (2.53 ± 0.23) nm for the first sample and (2.49 ± 0.21) nm for the drug loaded nanoparticles, indicating that most of the nanoparticles have a diameter of 5 nm in both cases. We observed a positive deviation of the experimental SAXS profiles from the model intensity for $q < 0.3$ nm^{-1}. The inspection of the Guinier plot (shown for the pristine AuNPs in the upper inset of Fig. 6a) and of the pair distance distribution functions obtained by indirect Fourier transform (Fig. 6b) also suggests that the samples contain a non-negligible fraction of particles with overall size larger than 5 nm. Allowing for a certain fraction of the spherical NPs to be structured within larger clusters, helped to fit the SAXS data at $q < 0.3$ nm^{-1} as well. The clusters were described by considering that a fraction of the spheres with 5 nm diameter is correlated by a fractal structure factor (fitting parameters reported in Tables S7-S8). The fractal dimension, the maximum distance for the correlations and the number density of spheres involved were best fitted to reproduce the SAXS data. The best-fit fractal dimension was 1.3 in

both cases, the maximum correlation size was 107 nm for pristine AuNPs and 65 nm for AuNPs-MTX, whereas the fraction of particles involved in clusters increased from 28% to 45% with addition of MTX, due to a decrease of the number of particles in the non-clustered population, as inferred form the distributions shown in the lower inset of Fig. 6a.

These overall values confirm what can be found with other characterisation techniques, such as DLS, SEM, and TEM measurements: the size of the gold nanoparticles does not relevantly change upon interaction with methotrexate, nor the presence of the drug triggers significant aggregation in the system.

In order to deeply understand the interaction with MTX, AuNPs before and after drug loading were studied by GISAXS and GIWAXS experiments at the P03 beamline (MINAXS), PETRA III in Hamburg. The influence of MTX on *inter-* and *intra-* particles degree of order was studied and in Fig. 6c the GISAXS and in Fig. 6d the GIWAXS scattering profiles of AuNPs and AuNPs-MTX are compared.

In the GISAXS profile of AuNPs (Fig. 6c) a peak centred at 1.134 nm^{-1} for pristine gold nanoparticles is found; this peak is shifted to lower q values (0.64 nm^{-1}) after the interaction with MTX. This could confirm the non-covalent interaction between the thiols and the drug, as the interparticle distance increases when MTX is added (5.54 nm for pristine AuNPs, 9.82 nm for AuNPs-MTX), suggesting the presence of the drug on the surface of the AuNPs, which would increase the size of the shell surrounding the metal core (see inset of Fig. 6c). GIWAXS scattering profiles, shown in Fig. 6d, show a Bragg peak centred at 26.8 nm^{-1} for pristine (1 1 1) AuNPs which substantially decreased and was slightly shifted to smaller *q*-values after drug interaction. A similar behaviour was found for the less prominent (2 0 0) peak at higher q values. Moreover, the lower intensity of the peak at about 22.5 nm^{-1} in Fig. 6d associated with interaction between the thiols is completely gone after MTX addition. This confirms a strong influence on interparticle arrangement and a certain loss in the internal order of the AuNPs after being exposed to the drug. 2D GISAXS and GIWAXS data are collected in Figure S6.
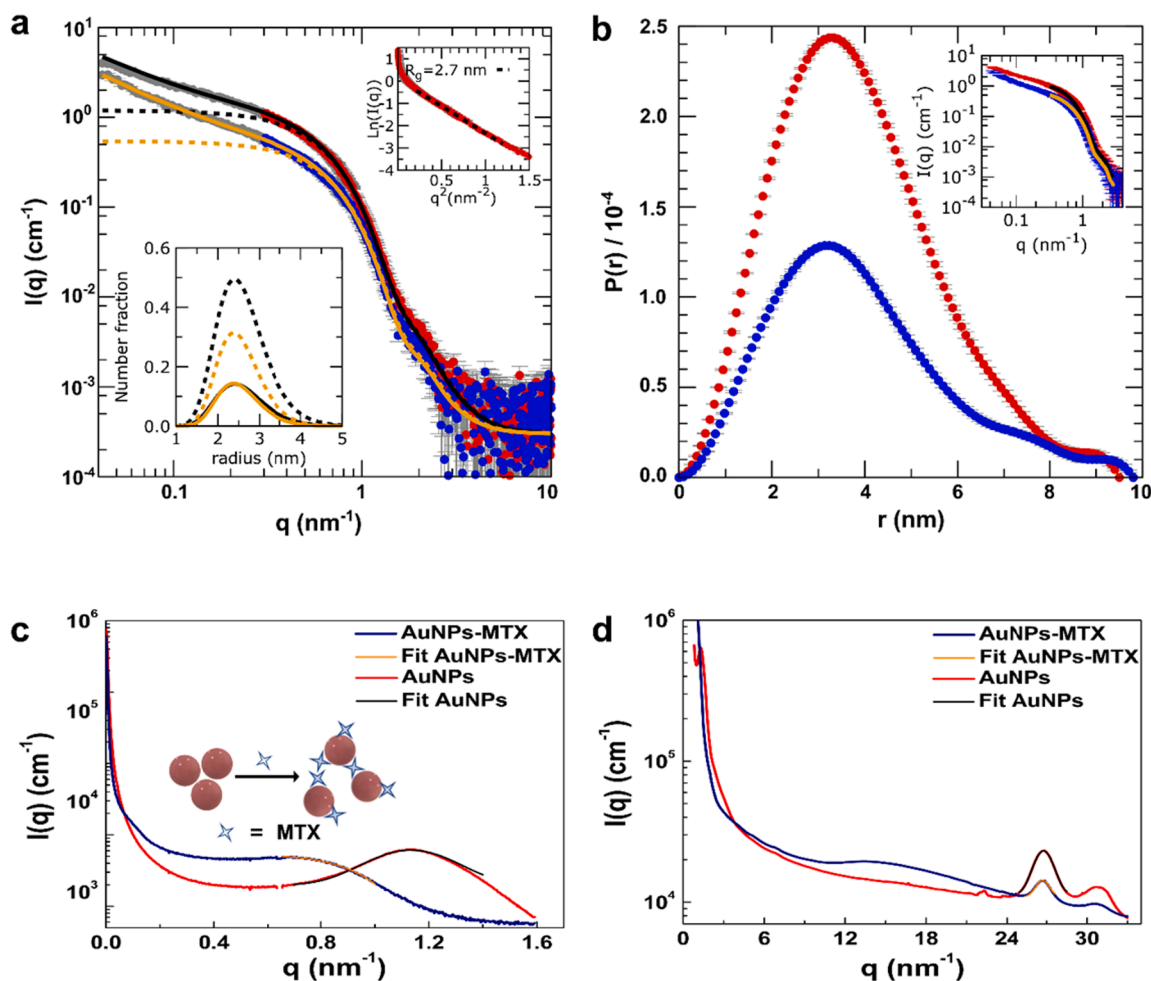
Fig. 6. a: SAXS profiles of AuNPs (red dots) and AuNPs-MTX (blue dots) with the relative best fit curves for a distribution of spheres (black and orange dotted curve, respectively). The fits considering a fraction of the spheres to be structured within < 100 nm clusters are reported as solid lines. The corresponding distributions for the sphere radius are shown in the lower inset. In the upper inset, the Guinier plot for AuNPs is shown together with the linear fit $\ln(I) = \ln(I_0)-(R_g/3)q^2$, according to a radius of gyration $R_g = 2.7$. b: Pair distance distribution functions obtained by indirect Fourier transform from tha AuNPs (red dots) and AuNPs-MTX (blue dots) SAXS data. The corresponding fits are shown in the inset. GISAXS superimposed profiles of AuNPs and AuNPs-MTX (c), GIWAXS superimposed profiles of pristine and drug loaded AuNPs (d). Best fits are superimposed on the curves. Inset of c: schematic depiction of AuNPs and AuNPs-MTX after the interaction. Peaks centres, GISAXS: pristine AuNPs, 1.13 nm^{-1}; AuNPs-MTX, 0.64 nm^{-1}; GIWAXS: pristine AuNPs, 26.8 nm^{-1}; AuNPs-MTX, 26.7 nm^{-1}. (For interpretation of the references to colour in this figure legend, the reader is referred to the web version of this article.)

3.3. Cell viability studies

Pristine and MTX loaded AuNPs were used to assess the cell viability on neuroblastoma SJNKP and IMR5 cell lines, by MTT assays. Tumour cells were selected based on previous studies, where a lower activity of the endocellular defence system of cancer cells with respect to normal cells was proven [40]. The treatment was performed with a higher concentration (17 µM) of MTX on AuNPs (see Figures S7, S8) and lower concentrations, in the 0.015–0.124 µM range, as shown in Fig. 7. SJNKP and IMR5 cells were treated for 48 h and cell viability was evaluated by MTT (Fig. 7 a,b). The number of seeded cells was 5×10^3 cells/well. All three concentrations of AuNPs loaded with the respective MTX concentrations show a significant effect, compared to both SJNKP and IMR5 control cells. The values ***p = 0.0005 and ***p = 0.0006 are obtained for 0.015 µM MTX on AuNPs 0.5 µg/mL, for SJNKP and IMR5, respectively, with cell viability (43.40 ± 2.8) % for SJNKP (number of cells 17360 ± 3140) and (52.03 ± 4.24) % for IMR5 (number of cells 20810 ± 5000); ***p = 0.0004 and ***p = 0.0003 are related to 0.031 µM on AuNPs 10 µg/mL for SJNKP and IMR5, respectively, with cell viability (42.38 ± 1.98) % for SJNKP (number of cells 16950 ± 2050) and (48.92 ± 2.13) % for IMR5 (number of cells 19570 ± 3730); ***p = 0.0007 and

***p = 0.0008 refer to 0.124 µM on AuNPs 50 µg/mL for SJNKP and IMR5, respectively, with cell viability (45.75 ± 5.59) % for SJNKP (number of cells 18300 ± 4130) and (52.90 ± 8.14) % for IMR5 (number of cells 21160 ± 5300). 0.015 µM free MTX didn't show any significant effect, compared to control cells, while 0.124 µM free MTX shows a significant effect compared to SJNKP and IMR5 control cells; ***p = 0.0005; ***p = 0.0009, respectively, with cell viability (44.11 ± 5.29) % for SJNKP (number of cells 17650 ± 3050) and (53.69 ± 3.04) % for IMR5 (number of cells 21480 ± 6870). The lowest concentration of AuNPs, loaded with 0.015 µM of MTX, show a significant effect compared to the free drug in both cell lines: ***p = 0.0004; **p = 0.002, respectively. 0.031 µM of MTX bound to 10 µg/mL of AuNPs shown a significant effect in reducing cell viability of SJNKP and IMR5 cells, compared to the free drug (0.031 µM) with *p = 0.02 and *p = 0.04, respectively. Free nanoparticles did not show any cytotoxic effect on SJNKP cell line, while a mild cytotoxic effect for the highest concentration (50 µg/mL) was observed on IMR5 cells, with *p = 0.03. This cytotoxicity occurred in small cases of experiments, which can be considered negligible for further studies. The treatment was performed also for 24 h (data not shown).

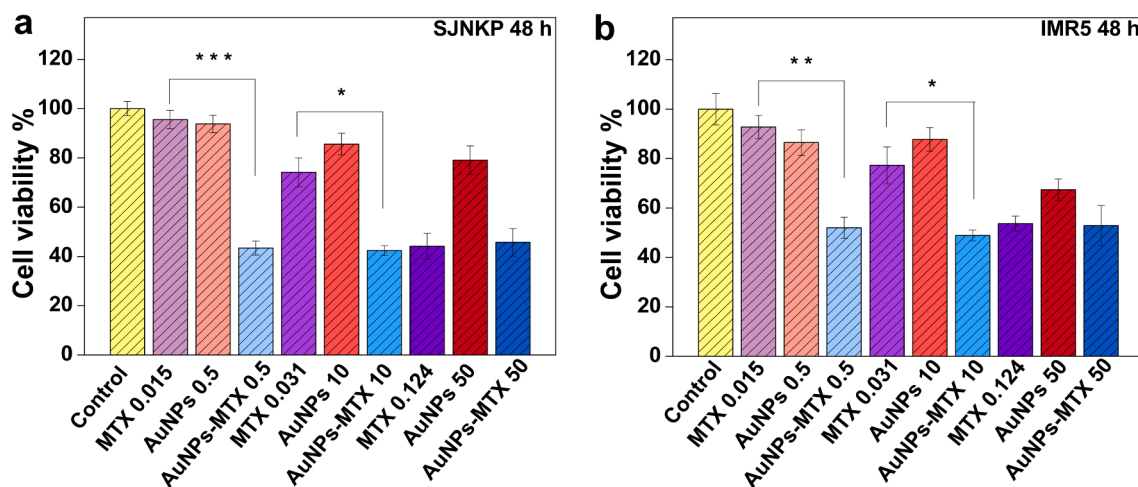A dose–response curve of MTX was also performed using an MTT

Fig. 7. a, b: MTT assays at 48 h for low MTX concentrations. The nanoconjugate is compared with pristine AuNPs and drug at three different AuNPs concentrations (0.5 μg/mL, 10 μg/mL, 50 μg/mL). MTX concentrations on AuNPs-MTX and free MTX are 0.015 μM, 0.031 μM, 0.124 μM; loaded on AuNPs 0.5 μg/mL, 10 μg/mL, 50 μg/mL, respectively; ***p = 0.0009 and **p = 0.004 are obtained for 0.015 μM MTX on AuNPs 0.5 μg/mL, for SJNKP and IMR5, respectively; *p = 0.03 and *p = 0.04 are related to 0.031 μM on AuNPs 10 μg/mL for SJNKP and IMR5, respectively.

assay (as reported in Figure S9) and the half maximal inhibitory concentration (IC50) was calculated (see Fig. 8). SJNKP were treated with several concentrations of MTX ranging from 0.001 to 50 μM. After 24 h (Figure S9), MTX started to show a significant cytotoxic effect at 0.05 μM with **p = 0.004 up to 50 μM with ****p = 0.0001. IC50 was calculated to be equal to 0.0793 μM (see Fig. 8a). This effect was maintained at 48 h, with a significant cytotoxic effect starting from 0.05 μM, **p = 0.003 with an IC50 of 0.0220 μM (Fig. 8b). In IMR5 cells, MTX showed a significant effect on cell viability reduction from 0.2 μM at 24 h (Figure S9); *p = 0.02 with an IC50 of 0.1080 μM (Fig. 8c). At 48 h this effect was already significant at 0.05 μM with ****p = 0.0001

(Figure S9), with an IC50 of 0.0318 μM (Fig. 8d). These results suggested to bind three different concentration of Methotrexate, 0.015 μM on AuNPs 0.5 μg/mL, 0.031 μM on AuNPs 10 μg/mL and 0.124 μM on AuNPs 50 μg/mL.

Concentrations of MTX loaded onto AuNPs in the range 0.015 – 0.031 μM induce a marked cytotoxic effect compared to the free MTX. Pristine AuNPs demonstrated to be prevalently not cytotoxic towards NB cell lines. Considering the high toxicity of MTX alone, this strategy allows to deliver a lower amount of the drug, following a synergic and potentiated effect upon loading.

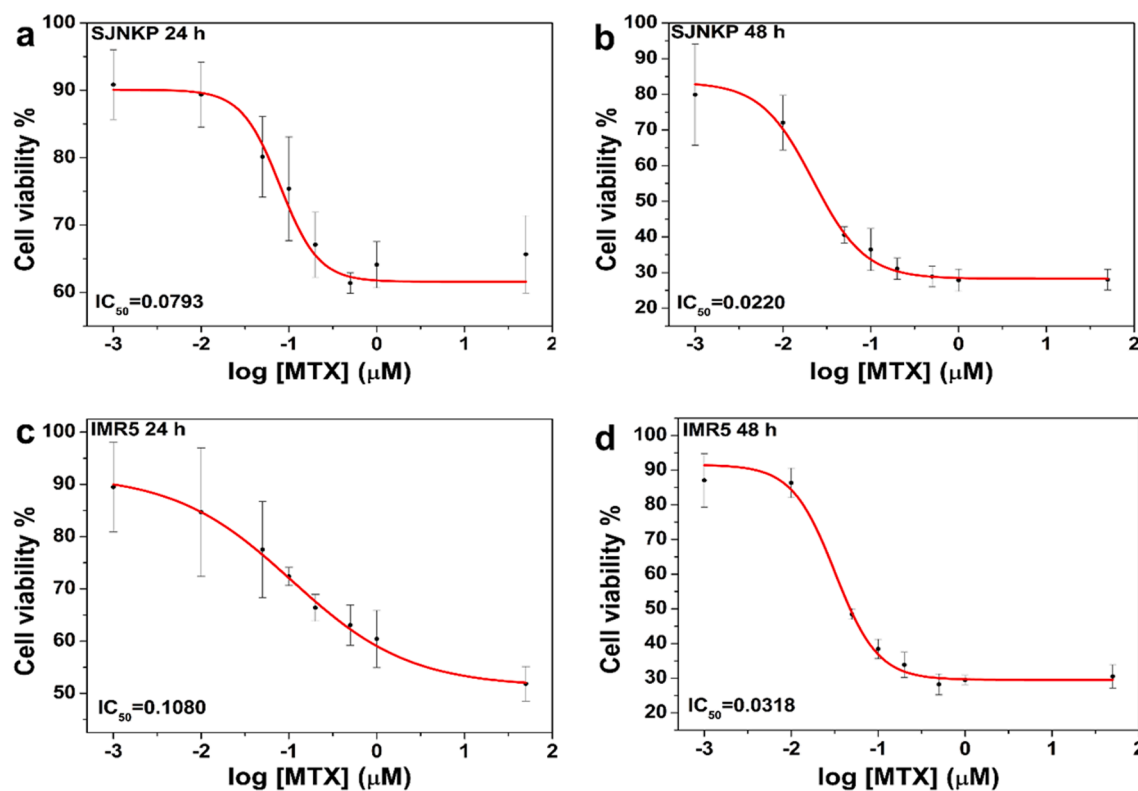These results suggest a new and promising therapeutic approach in

Fig. 8. Dose-response curves of MTX, SJNKP (a,b) and IMR5 (c,d) cell lines were treated at 24 h and 48 h with increasing MTX concentration. SJNKP cells after 24 h: IC50 = 0.0793 μM; after 48 h IC50 = 0.0220 μM. IMR5 cells after 24 h, IC50 = 0.1080 μM; after 48 h, IC50 = 0.0318 μM).

clinical applications for the for the treatment of neuroblastoma tumours. Further studies will be performed to investigate the localisation of this nanosystem in neuroblastoma tumour mass and the biochemical and molecular mechanism of cytotoxicity.

3.4. Direct imaging evidence of AuNPs uptaken by cells

Direct imaging TEM observations confirms the potential ability of the AuNPs to be well sequestered by IMR5 cells (Fig. 9). Smallest aggregates of dark nanoparticles distributed around the perinuclear region are displayed in the magnified image of bright-field TEM image (Fig. 9b). To identify experimentally the internalised nanoparticles, selected area electron diffraction (SAED) experiments were carried out. This allowed to characterise the atomic and structural compositions of the nanoconjugates. The electron diffraction pattern (EDP) shows two weak diffraction rings produced by the polycrystalline material in a random orientation (Fig. 9c). The weak diffraction signal is due to the high diffusion beam of the resin, embedding the cell. By measuring the d-spacing of the diffraction rings, we were able to identify the face-centred-cubic (fcc) Au with a space group *Fm3m* of the (1 1 1) and (2 0 0) Au reflections (yellow dot line arcs). To visualize the crystalline feature of the AuNPs, dark-field (DF) imaging was applied. DF images have been obtained by placing the objective aperture around both diffracted beams of the Debye rings (white circle of Fig. 9c). Therefore, the DF image well shows bright dots in Fig. 9d, having same position in Fig. 9b (dark dots) and confirming experimentally the golden nature of the nanoparticles. The smallest nanoparticles, efficiently uptake by cell, are observed either isolated or nanoaggregate states probably dependent from the internalization mechanisms of the engaged biological processes.

The permeation of AuNPs inside the cell membrane was evaluated *via* UV–vis; absorbance intensity of AuNPs and AuNPs-MTX supernatant solution after 24 and 48 h of MTT assay were compared to the intensity of the stock AuNPs solution (Fig. 10). By doing so, it was possible to infer by difference the relative quantity of AuNPs that permeated inside the cells at 24 and 48 h. As seen in Fig. 10a,b, IMR5 cells showed a higher permeation of AuNPs-MTX compared to pristine AuNPs (24 h: 25% AuNPs, 63% AuNPs-MTX; 48 h: 54% AuNPs, 73% AuNPs-MTX), at both time points. The same behaviour can be observed for SJNKP cells, see Fig. 10c,d (24 h: 57% AuNPs, 67% AuNPs-MTX; 48 h: 58% AuNPs, 70% AuNPs-MTX). This experiment suggests that the synergistic effect of the small size of the hydrophilic nanoparticles, together with the presence of an antifolate drug, increases the absorption of the probe by the cells.

4. Conclusions

Highly hydrophilic, small, stable, and non-cytotoxic AuNPs as drug

carriers have a promising potential for their use against cancer. In this work, a lipophilic drug was loaded on hydrophilic nanoparticles, thus increasing its bioavailability [23,38]. The choice of direct functionalisation with highly hydrophilic thiols greatly decreases the possible cytotoxicity of the gold nanoparticles, as well as the chance of biofouling from the body [33]. Methotrexate, an anti-folate drug, was loaded on the AuNPs, yielding a high loading percentage, while the system remained stable after the interaction between the surface thiols and MTX. The pristine and loaded system was characterised with several and advanced techniques, highlighting its colloidal stability and reduced size of the nanoparticles, key factors for their use as drug delivery probes. The drug loaded system was studied to confirm the stability of the system after the interaction with MTX, and to thoroughly assess the type of non-covalent interaction between the surface thiols and the drug. Combining dispersed phase and solid-state studies, such as ζ-potential, NMR, XPS and FTIR, we proposed a twofold nature of the interface interaction between surface thiols and drug: electrostatic and cation-π. Results of solid-state GIWAXS/GISAXS and SAXS carried out on colloidal dispersions gave structural information about the different behaviour of the loaded and pristine system in different hydration states. The systems were tested *in vitro* towards two different neuroblastoma cell lines, SJNKP and IMR5 with overexpressed *n*-Myc. Pristine AuNPs showed no significant cytotoxic effect in both cell lines, whereas AuNPs-MTX showed a stronger cytotoxic effect when compared to free MTX at the same concentration. A permeation effect mediated by the hydrophilic AuNPs in the cells was found to improve the penetration of MTX inside the cells. Further studies should be carried out to test the system for *in vivo* studies on neuroblastoma tumour masses.

CRediT authorship contribution statement

Tommaso A. Salamone: Conceptualization, Investigation, Methodology, Data curation, Formal analysis, Funding acquisition, Visualization, Writing – original draft, Writing – review & editing. **Lavinia Rutigliano:** Visualization, Conceptualization. **Beatrice Pennacchi:** Investigation, Methodology, Data curation, Visualization. **Sara Cerra:** Investigation, Methodology, Data curation, Visualization. **Roberto Matassa:** Investigation, Methodology, Data curation, Visualization. **Stefania Nottola:** Investigation, Methodology, Data curation, Visualization. **Fabio Sciubba:** Investigation, Methodology, Data curation, Visualization. **Chiara Battocchio:** Investigation, Methodology, Data curation, Visualization. **Martina Marsotto:** Investigation, Methodology, Data curation, Visualization. **Alessandra Del Giudice:** Investigation, Methodology, Data curation, Visualization. **Andrei Chumakov:** Investigation, Methodology, Data curation, Visualization. **Anton Davydok:** Investigation, Methodology, Data curation, Visualization. **Souren Grigorian:** Conceptualization, Investigation, Methodology, Data curation,
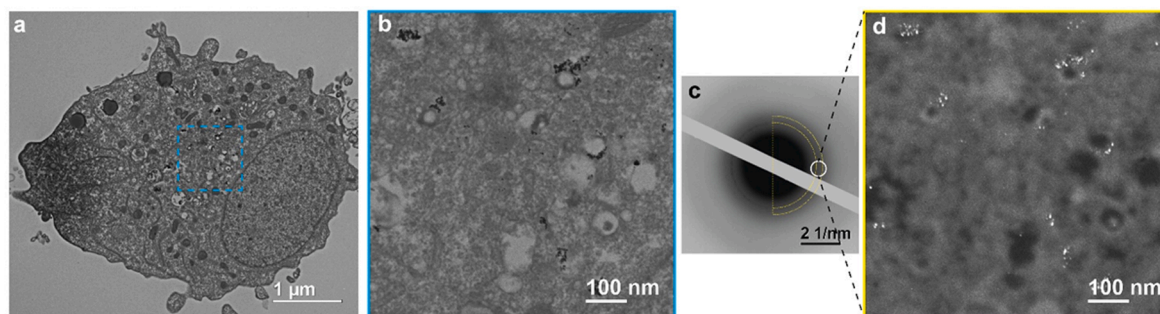
Fig. 9. Morphostructural observations of AuNPs uptake by neuroblastoma cells. (a) Cross-section of IMR5 cell with smallest AuNPs nanoaggregates internalised near perinuclear region (blue dot line square) and (b) the corresponding magnified area. (c) EDP taken from Fig. 9b) shows diffraction rings belonging to the face-centred-cubic Au phase (yellow dot line arcs). (d) DF TEM image of Fig. 9a) obtained by selecting both reflections of (1 1 1) and (2 0 0) of the AuNPs, labelled by a white circle in Fig. 9c). Intense white spots belong to smallest Au nanoparticles. (For interpretation of the references to colour in this figure legend, the reader is referred to the web version of this article.)
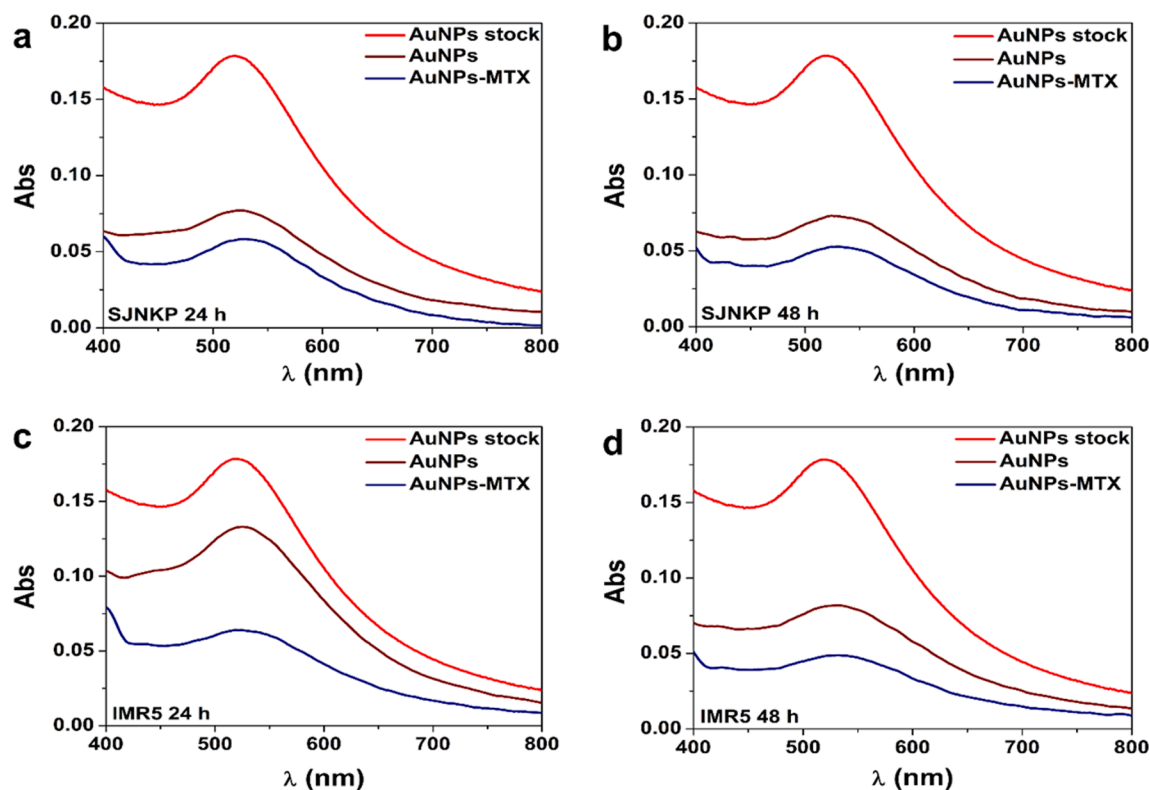
Fig. 10. UV–visible spectra of AuNPs (dark red) and AuNPs-MTX (blue) compared to AuNPs stock solution (red) permeation tests, at different time points (24 and 48 h) on SJNKP (a), b)) and IMR5 (c), d)) cell lines. (For interpretation of the references to colour in this figure legend, the reader is referred to the web version of this article.)

Declaration of Competing Interest

The authors declare that they have no known competing financial interests or personal relationships that could have appeared to influence the work reported in this paper.

Data availability

Data will be made available on request.

Acknowledgements

Appendix A. Supplementary data

Supplementary data to this article can be found online at https://doi.org/10.1016/j.jcis.2023.06.078.

References

[1] O.O. Havryliuk, A.A. Evtukh, O.V. Pylypova, O.Y. Semchuk, I.I. Ivanov, V. F. Zabolotnyi, Plasmonic enhancement of light to improve the parameters of solar cells, Appl. Nanosci. 10 (2020) 4759–4766, https://doi.org/10.1007/s13204-020-01299-w.

[2] S. Cerra, T.A. Salamone, F. Sciubba, M. Marsotto, C. Battocchio, S. Nappini, F. A. Scaramuzzo, V.R. Li, C. Sibilia, R. Matassa, A.M. Beltrán, G. Familiari, Study of the interaction mechanism between hydrophilic thiol capped gold nanoparticles and melamine in aqueous medium, Colloids Surf. B 203 (2021) 111727, https://doi.org/10.1016/j.colsurfb.2021.111727.

[3] T.H.A. Nguyen, T.T.V. Le, B.A. Huynh, N.V. Nguyen, V.T. Le, V.-D. Doan, V. A. Tran, A.-T. Nguyen, X.T. Cao, Y. Vasseghian, Novel biogenic gold nanoparticles stabilized on poly(styrene-co-maleic anhydride) as an effective material for reduction of nitrophenols and colorimetric detection of Pb(II), Environ. Res. 212 (2022) 113281, https://doi.org/10.1016/j.envres.2022.113281.

[4] J. Beik, M. Khateri, Z. Khosravi, S.K. Kamrava, S. Kooranifar, H. Ghaznavi, A. Shakeri-Zadeh, Gold nanoparticles in combinatorial cancer therapy strategies, Coord. Chem. Rev. 387 (2019) 299–324, https://doi.org/10.1016/j.ccr.2019.02.025.

[5] E.C. Dreaden, A.M. Alkilany, X. Huang, C.J. Murphy, M.A. El-Sayed, The golden age: gold nanoparticles for biomedicine, Chem. Soc. Rev. 41 (2012) 2740–2779, https://doi.org/10.1039/C1CS15237H.

[6] A.M. Alam, Y.S. Shon, Water-soluble noble metal nanoparticle catalysts capped with small organic molecules for organic transformations in water, ACS Appl. Nano Mater. 4 (4) (2021) 3294–3318, https://doi.org/10.1021/acsanm.1c00335.

[7] K. Sztandera, M. Gorzkiewicz, B. Klajnert-Maculewicz, Gold Nanoparticles in Cancer Treatment, Mol. Pharm. 16 (2019) 1–23, https://doi.org/10.1021/acs.molpharmaceut.8b00810.

[8] Y. Jiang, W. Zhao, H. Zhou, Q. Zhang, S. Zhang, ATP-Triggered Intracellular in Situ Aggregation of a Gold Nanoparticle-Equipped Triple-Helix Molecular Switch for

Fluorescence Imaging and Photothermal Tumor Therapy, Langmuir 38 (2022) 3755–3764, https://doi.org/10.1021/acs.langmuir.1c03331.

[9] S. Luan, R. Xie, Y. Yang, X. Xiao, J. Zhou, X. Li, P. Fang, X. Zeng, X. Yu, M. Chen, H. Gao, Y. Yuan, Acid-Responsive Aggregated Gold Nanoparticles for Radiosensitization and Synergistic Chemoradiotherapy in the Treatment of Esophageal Cancer, Small 18 (2022) 2200115, https://doi.org/10.1002/smll.202200115.

[10] N. Bertrand, J. Wu, X. Xu, N. Kamaly, O.C. Farokhzad, Cancer nanotechnology: The impact of passive and active targeting in the era of modern cancer biology 66 (2014) 2–25, https://doi.org/10.1016/j.addr.2013.11.009.

[11] I. Venditti, A. Cartoni, S. Cerra, R. Fioravanti, T.A. Salamone, F. Sciubba, M. A. Tabocchini, V. Dini, C. Battocchio, G. Iucci, L. Carlini, R. Faccini, F. Collamati, T. C. Mancini, C.E. Solfaroli, S. Morganti, A. Giordano, T. Scotognella, D. Maccora, D. Rotili, C. Marchese, E. Anastasiadou, P. Trivedi, I. Fratoddi, Hydrophilic Gold Nanoparticles as Anti-PD-L1 Antibody Carriers: Synthesis and Interface Properties, Part. Part. Syst. Charact. 39 (2022) 2100282, https://doi.org/10.1002/ppsc.202100282.

[12] R. Terracciano, Y. Carcamo-Bahena, A.L.R. Royal, L. Messina, J. Delk, E.B. Butler, D. Demarchi, A. Grattoni, Z. Wang, V. Cristini, P. Dogra, C.S. Filgueira, Zonal Intratumoral Delivery of Nanoparticles Guided by Surface Functionalization, Langmuir 38 (2022) 13983–13994.

[13] S. Dixit, T. Novak, K. Miller, Y. Zhu, M.E. Kenney, A.-M. Broome, Transferrin receptor-targeted theranostic gold nanoparticles for photosensitizer delivery in brain tumors, Nanoscale 7 (2014) 1782–1790, https://doi.org/10.1039/c4nr04853a.

[14] F. Yu, J. Huang, Y. Yu, Y. Lu, Y. Chen, H. Zhang, G. Zhou, Z. Sun, J. Liu, D. Sun, G. Zhang, H. Zou, Y. Zhong, Glutathione-Responsive Multilayer Coated Gold Nanoparticles for Targeted Gene Delivery, J. Biomed. Nanotech. 12 (2016) 503–515, https://doi.org/10.1166/jbn.2016.2177.

[15] Z. Li, Y. Liu, X. Huang, C. Hu, H. Wang, L. Yuan, J.L. Brash, H. Chen, One-step preparation of gold nanovectors using folate modified polyethylenimine and their use in target-specific gene transfection, Colloids Surf. B Biointerfaces 177 (2019) 306–312, https://doi.org/10.1016/j.colsurfb.2019.02.011.

[16] N.G. Chabloz, H.L. Perry, I.C. Yoon, A.J. Coulson, A.J. White, G.J. Stasiuk, R.M. Botnar, J.D. Wilton-Ely, Combined Magnetic Resonance Imaging and Photodynamic Therapy Using Polyfunctionalised Nanoparticles Bearing Robust Gadolinium Surface Units, Chem. Eur. J., 26, (2020), 4552-4566 https://doi.org/10.1002/chem.201904757.

[17] H.S. Kim, M. Seo, T.-E. Park, D.Y. Lee, A novel therapeutic strategy of multimodal nanoconjugates for state-of-the-art brain tumor phototherapy, J. Nanobiotechnology 20 (2022) 14, https://doi.org/10.1186/s12951-021-01220-9.

[18] L. Yue, K. Yang, J. Wei, M. Xu, C. Sun, Y. Ding, Z. Yuan, S. Wang, R. Wang, Supramolecular Vesicles Based on Gold Nanorods for Precise Control of Gene Therapy and Deferred Photothermal Therapy, CCS Chemistry 4 (2022) 1745–1757. https://doi.org/10.31635/ccschem.021.202101029.

[19] K. Kalimuthu, B.-C. Lubin, A. Bazylevich, G. Gellerman, O. Shpilberg, G. Luboshits, M.A. Firer, Gold nanoparticles stabilize peptide-drug-conjugates for sustained targeted drug delivery to cancer cells, J. Nanobiotechnology 16 (2018) 34, https://doi.org/10.1186/s12951-018-0362-1.

[20] Y. Wang, Y. Wen, Y. Qu, Z. Pei, Y. Pei, Pillar[5]arene based glyco-targeting nitric oxide nanogenerator for hyperthermia-induced triple-mode cancer therapy, J. Colloid Interface Sci 615 (2022) 386–394, https://doi.org/10.1016/j.jcis.2022.01.189.

[21] S. Lorenzoni, S. Cerra, E. Angulo-Elizari, T.A. Salamone, C. Battocchio, M. Marsotto, F.A. Scaramuzzo, C. Sanmartín, Organoselenium compounds as functionalizing agents for gold nanoparticles in cancer therapy, Colloids Surf. B 219 (2022), 112828, https://doi.org/10.1016/j.colsurfb.2022.112828.

[22] B. Singh, C. Patnaik, R. Bahadur, M. Gandhi, A. De, R. Srivastava, Synthesis and degradation mechanism of renally excretable gold core–shell nanoparticles for combined photothermal and photodynamic therapy, Nanoscale 15 (2023) 1273–1288, https://doi.org/10.1039/D2NR05283K.

[23] A.M. Cryer, C. Chan, A. Eftychidou, C. Maksoudian, M. Mahesh, T.D. Tetley, A. C. Spivey, A.J. Thorley, Tyrosine kinase inhibitor gold nanoconjugates for the treatment of non-small cell lung cancer, ACS Appl. Mater. Interfaces 11 (2019) 16336–16346, https://doi.org/10.1021/acsami.9b02986.

[24] S.D. Brown, P. Nativo, J.-A. Smith, D. Stirling, P.R. Edwards, B. Venugopal, D. J. Flint, J.A. Plumb, D. Graham, N.J. Wheate, Gold nanoparticles for the improved anticancer drug delivery of the active component of oxaliplatin, J. Am. Chem. Soc. 132 (2010) 4678–4684, https://doi.org/10.1021/ja908117a.

[25] Y. Cheng, J.D. Meyers, A.M. Broome, M.E. Kenney, J.P. Basilion, C. Burda, Deep Penetration of a PDT Drug into Tumors by Noncovalent Drug-Gold Nanoparticle Conjugates, J. Am. Chem. Soc. 133 (2011) 2583–2591, https://doi.org/10.1021/ja108846h.

[26] L.M. Liz-Marzán, Gold nanoparticle research before and after the Brust-Schiffrin method, Chem. Commun. 49 (2013) 16–18, https://doi.org/10.1039/c2cc35720h.

[27] A. Ulman, Formation and structure of self-assembled monolayers, Chem. Rev. 96 (1996) 1533–1554, https://doi.org/10.1021/cr9502357.

[28] S. Dey, K. Sreenivasan, Conjugating curcumin to water soluble polymer stabilized gold nanoparticles via pH responsive succinate linker, J. Mater. Chem. B 3 (2015) 824–833, https://doi.org/10.1039/c4tb01731e.

[29] F. Porcaro, C. Battocchio, A. Antoccia, I. Fratoddi, I. Venditti, A. Fracassi, I. Luisetto, M.V. Russo, G. Polzonetti, Synthesis of Functionalized Gold Nanoparticles Capped with 3-Mercapto-1-Propansulfonate and 1-Thioglucose Mixed Thiols and "in Vitro" Bioresponse, Colloids Surf. B 142 (2016) 408–416, https://doi.org/10.1016/j.colsurfb.2016.03.016.

[30] Y. Feng, X. Li, D. Ji, J. Tian, Q. Peng, Y. Shen, Y. Xiao, Functionalised penetrating peptide-chondroitin sulphate–gold nanoparticles: Synthesis, characterization, and applications as an anti-Alzheimer's disease drug, Int. J. Biol. Macromol. 230 (2023), 123125, https://doi.org/10.1016/j.ijbiomac.2022.123125.

[31] S. Chatterjee, X.-Y. Lou, F. Liang, Y.-W. Yang, Surface-functionalized gold and silver nanoparticles for colorimetric and fluorescent sensing of metal ions and biomolecules, Coord. Chem. Rev. 459 (2022), 214461, https://doi.org/10.1016/j.ccr.2022.214461.

[32] S. Farhangi, E. Karimi, K. Khajeh, S. Hosseinkhani, M. Javan, Peptide mediated targeted delivery of gold nanoparticles into the demyelination site ameliorates myelin impairment and gliosis, Nanomed.: Nanotechnol. Biol. Med, 47, (2023), 102609, https://doi.org/10.1016/j.nano.2022.102609.

[33] R. Terracciano, Y. Carcamo-Bahena, E.B. Butler, D. Demarchi, A. Grattoni, C. S. Filgueira, Hyaluronate-thiol passivation enhances gold nanoparticle peritumoral distribution when administered intratumorally in lung cancer, Biomedicines 9 (2021) 1561, https://doi.org/10.3390/biomedicines9111561.

[34] P. Mishra, B. Nayak, R.K. Dey, PEGylation in Anti-Cancer Therapy: An Overview, Asian J. Pharm. Sci. 11 (2016) 337–348, https://doi.org/10.1016/j.ajps.2015.08.011.

[35] M. Ponzoni, T. Bachetti, M.V. Corrias, C. Brignole, F. Pastorino, E. Calarco, V. Bensa, E. Giusto, I. Ceccherini, P. Perri, Recent advances in the developmental origin of neuroblastoma: an overview, J. Exp. Clin. Cancer Res. 41 (2022) 92, https://doi.org/10.1186/s13046-022-02281-w.

[36] S. Cerra, R. Matassa, A.M. Beltrán, G. Familiari, C. Battocchio, I. Pis, F. Sciubba, F. A. Scaramuzzo, A. Del Giudice, I. Fratoddi, Insights about the interaction of methotrexate loaded hydrophilic gold nanoparticles: Spectroscopic, morphological and structural characterizations, Mater. Sci. Eng. C 117 (2020), 111337, https://doi.org/10.1016/j.msec.2020.111337.

[37] I. Fratoddi, L. Benassi, E. Botti, C. Vaschieri, I. Venditti, H. Bessar, M.A. Samir, P. Azzoni, C. Magnoni, A. Costanzo, V. Casagrande, M. Federici, Effects of topical methotrexate loaded gold nanoparticle in cutaneous inflammatory mouse model, Nanomed.: Nanotechnol, Biol. Med. 17 (2019) 276–286, https://doi.org/10.1016/j.nano.2019.01.006.

[38] Z. Taran, S.Y. Digehsaraei, M. Salouti, B. Amini, S. Mahmazi, M. Kalantari, Methotrexate loaded in alginate beads for controlled drug release against breast cancer, Gene 851 (2023), 146941, https://doi.org/10.1016/j.gene.2022.146941.

[39] M. Yang-Bao, Z. Wang, R. Gao, G. Ying, S. Yi, Customizing delivery nano-vehicles for precise brain tumor therapy, J. Nanobiotechnology 21 (2023) 32, https://doi.org/10.1186/s12951-023- 01775-9.

[40] Y. Kanamori, A. Finotti, L. Di Magno, G. Canettieri, T. Tahara, F. Timeus, A. Greco, P. Tirassa, J. Gasparello, P. Fino, C.M. Di Liegro, P. Proia, G. Schiera, I. Di Liegro, R. Gambari, E. Agostinelli, Enzymatic Spermine Metabolites Induce Apoptosis Associated with Increase of p53, caspase-3 and miR-34a in Both Neuroblastoma Cells, SJNKP and the N-Myc-Amplified Form IMR5, Cells 10 (2021) 1950–1975, https://doi.org/10.3390/cells10081950.

[41] J. Hayes, P.P. Peruzzi, S. Lawler, MicroRNAs in cancer: Biomarkers, functions and therapy, Trends Mol. Med. 20 (2014) 460–469, https://doi.org/10.1016/j.molmed.2014.06.005.

[42] A. Buffet, A. Rothkirch, R. Döhrmann, V. Körstgens, M.M. Abul Kashem, J. Perlich, G. Herzog, M. Schwartzkopf, R. Gehrke, P. Müller-Buschbaum, S.V. Roth, P03, the Microfocus and Nanofocus X-Ray Scattering (MiNaXS) Beamline of the PETRA III Storage Ring: The Microfocus Endstation, J. Synchrotron Radiat. 19 (2012) 647–653, https://doi.org/10.1107/S0909049512016895.

[43] G. Benecke, W. Wagermaier, C. Li, M. Schwartzkopf, G. Flucke, R. Hoerth, I. Zizak, M. Burghammer, E. Metwalli, P. Müller-Buschbaum, M. Trebbin, S. Förster, O. Paris, S.V. Roth, P. Fratzl, A Customizable Software for Fast Reduction and Analysis of Large X-Ray Scattering Data Sets: Applications of the New DPDAK Package to Small-Angle X-Ray Scattering and Grazing-Incidence Small-Angle X-Ray Scattering, J. Appl. Crystallogr. 47 (2014) 1797–1803, https://doi.org/10.1107/S1600576714019773.

[44] C.T. Singley, M. Solursh, The use of tannic acid for the ultrastructural visualization of hyaluronic acid, Histochemistry 65 (1980) 93–102, https://doi.org/10.1007/BF00493158.

[45] G. Reina, E. Tamburri, S. Orlanducci, S. Gay, R. Matassa, V. Guglielmotti, T. Lavecchia, M.L. Terranova, M. Rossi, Nanocarbon surfaces for biomedicine, Biomatter 4 (2014) e28537.

[46] M.F. Peralta, S.N. Mendieta, I.R. Scolari, G.E. Granero, M.E. Crivello, Synthesis and release behavior of layered double hydroxides–carbamazepine composites, Sci Rep 11 (2021) 20585, https://doi.org/10.1038/s41598-021-00117-9.

[47] T. Mosmann, Rapid colorimetric assay for cellular growth and survival: application to proliferation and cytotoxicity assays, J. lmmunol. Methods 65 (1983) 55–63, https://doi.org/10.1016/0022-1759(83)90303-4.

[48] Y. Kanamori, L.D. Via, A. Macone, G. Canettieri, A. Greco, A. Toninello, E. Agostinelli, Aged garlic extract and its constituent, S-allyl-L-cysteine, induce the apoptosis of neuroblastoma cancer cells due to mitochondrial membrane depolarization, Exp. Ther. Med. 19 (2020) 1511–1521, https://doi.org/10.3892/etm.2019.8383.

[49] M. Brust, M. Walker, D. Bethell, D.J. Schiffrin, R. Whyman, Synthesis of thiol-derivatised gold nanoparticles in a two-phase liquid-liquid system, ChemComm 7 (1994) 801–802, https://doi.org/10.1039/C39940000801.

[50] S.K. Ghosh, T. Pal, Interparticle Coupling Effect on the Surface Plasmon Resonance of Gold Nanoparticles: From Theory to Applications, Chem. Rev. 107 (2007) 4797–4862, https://doi.org/10.1021/cr0680282.

[51] M. Yu, J. Zheng, Clearance Pathways and Tumor Targeting of Imaging Nanoparticles, ACS Nano 9 (2015) 6655–6674, https://doi.org/10.1021/acsnano.5b01320.

[52] M. İlgar, S. Karakuş, A. Kilislioğlu, Design, characterization and evaluation of the drug–loaded chitosan/cerium oxide nanoparticles with pH–controlled drug release, Polym. Bull. 79 (2022) 6693–9708, https://doi.org/10.1007/s00289-021-03839-y.

[53] I. Cooper, M. Fridkin, Y. Shechter, Conjugation of Methotrexate-Amino Derivatives to Macromolecules through Carboxylate Moieties Is Superior Over Conventional Linkage to Amino Residues: Chemical, Cell-Free and *In Vitro* Characterizations, PLoS One 11 (2016) e0158352.

[54] R. Silverstein, F. Webster, D. Kiemle, Infrared Spectrometry, in: R. Silverstein, F. Webster, D. Kiemle (Eds.), Spectrometric identification of organic compounds, 7th ed., Wiley, Hoboken, USA, 2005, pp. 72–126.

[55] I. Venditti, G. Iucci, I. Fratoddi, M. Cipolletti, E. Montalesi, M. Marino, V. Secchi, C. Battocchio, Direct Conjugation of Resveratrol on Hydrophilic Gold Nanoparticles: Structural and Cytotoxic Studies for Biomedical Applications, Nanomaterials 10 (2020) 1898, https://doi.org/10.3390/nano10101898.

[56] I. Venditti, G. Testa, F. Sciubba, L. Carlini, F. Porcaro, C. Meneghini, S. Mobilio, C. Battocchio, I. Fratoddi, Hydrophilic Metal Nanoparticles Functionalized by 2-Diethylaminoethanethiol: A Close Look at the Metal-Ligand Interaction and Interface Chemical Structure, J. Phys. Chem. C 121 (2017) 8002–8013, https://doi.org/10.1021/acs.jpcc.7b01424.

[57] A. Najdian, M. Shakourian-Fard, A. Fattahi, Cooperativity effects of intramolecular OH...O interactions on pK_a values of polyolalkyl sulfonic acids in the gas phase and solution: A density functional theory study, J. Phys. Org. Chem. 27 (2014) 604–612, https://doi.org/10.1002/poc.3307.

[58] A.V. Rayer, K.Z. Sumon, L. Jaffari, A. Henni, Dissociation Constants (pKa) of Tertiary and Cyclic Amines: Structural and Temperature Dependences, J. Chem. Eng. Data 59 (2014) 3805–3813, https://doi.org/10.1021/je500680q.

[59] I. Venditti, L. Fontana, I. Fratoddi, C. Battocchio, C. Cametti, S. Sennato, F. Mura, F. Sciubba, M. Delfini, M.V. Russo, Direct interaction of hydrophilic gold nanoparticles with dexamethasone drug: Loading and release study, J. Colloid Interface Sci. 418 (2014) 52–60, https://doi.org/10.1016/j.jcis.2013.11.063.

[60] M. Kluenker, M. Mondeshki, T.M. Nawaz, W. Tremel, Monitoring Thiol-Ligand Exchange on Au Nanoparticle Surfaces, Langmuir 34 (2018) 1700–1710, https://doi.org/10.1021/acs.langmuir.7b04015.

[61] H.R. Masoodi, S. Bagheri, Interplay between π···π and cation···π interaction: a theoretical NMR study, J. Iran Chem. Soc. 12 (2015) 1883–1892, https://doi.org/10.1007/s13738-015-0663-3.

[62] D. Wei, F. Ma, R. Wang, S. Dou, P. Cui, H. Huang, J. Ji, E. Jia, X. Jia, S. Sajid, A. M. Elseman, L. Chu, Y. Li, B. Jiang, J. Qiao, Y. Yuan, M. Li, Ion-Migration Inhibition by the Cation–π Interaction in Perovskite Materials for Efficient and Stable Perovskite Solar Cells, Adv. Mater. 30 (2018) 1707583, https://doi.org/10.1002/adma.201707583.